Measurement of the Mass Flow and Tangential Momentum Accommodation Coefficient in Silicon Micromachined Channels

by

Errol B. Arkilic

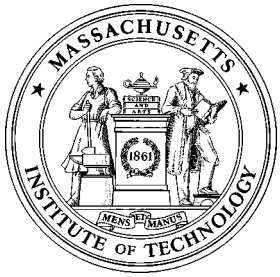

FDRL TR 97-1

Fluid Dynamics Research Laboratory
Department of Aeronautics and Astronautics
Massachusetts Institue of Technology
Cambridge, MA 02139

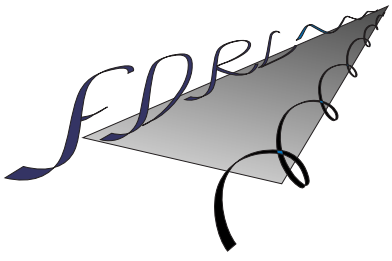

January, 1997

Abstract

An analytic and experimental investigation into gaseous flow with slight rarefaction through long microchannels is undertaken in an attempt to obtain values of the Tangential Momentum Accommodation Coefficient (TMAC) for a common MicroElectroMechanical Systems (MEMS) surface. A set of analytic expressions is developed from the slip-flow solutions of the Navier Stokes equations which can be used to interpret the results of flow in micromachined channels and to extract TMAC values from these results. In addition to the theoretical framework, a robust microchannel fabrication procedure and a dedicated high-resolution mass flow measurement technique is developed. These are used in conjunction to obtain TMAC values for single-crystal silicon upon which a native oxide resides for gas flows of argon, nitrogen and carbon dioxide. It is shown that the TMAC for this common MEMS surface can possess a value less than unity (0.75-0.85) for the conditions which are expected to be encountered with state-of-the-art MEMS.

This report is the Ph.D. Thesis of Errol B. Arkilic, Submitted to the Department of Aeronautics and Astronautics, M.I.T. in December, 1996, Supervised by Profs. Kenneth Breuer and Martin Schmidt. For more information, contact, Prof. K. Breuer: `breuer@mit.edu`

Acknowledgments

It is impossible to acknowledge all of the contributions and support which I have received while working on the research behind this thesis and any attempt at full inclusion would certainly be lacking. Nonetheless, there are some contributions which stand out in my mind.

To begin, financial support for this work was provided under DARPA contract #J-FB1-92-196 and Marty Schmidt's NSF Presidential Young Investigators award. Additional support for various hardware was provided for by AFOSR under contract #F49620-93-1-0194, monitored by James McMichael. Also, during the writing of this thesis I was supported by Physical Science Incorporated.

Among the people I have to thank, my advisors, Kenny Breuer and Marty Schmidt stand out. Kenny has been a consistent source of intellectual wealth and his inquisitive nature is contagious. Furthermore, he has always been willing to lend an ear as well as provide suggestions during times of intense technical challenge. Marty has been the source of deep technical knowledge as well. However, it is his direction and kind words of encouragement during difficult times as well as his frank and sagacious advise that I am most appreciative of.

Among my other committee members, Harold Wachman has significantly contributed to the intellectual content of this thesis. Furthermore, his vast knowledge of gas-surface interactions as well as rarefied gas dynamics have provided a framework with which to view the contributions of this research. I am also appreciative of the contributions of David Gonzales. Along the way, David has posed several probing questions which, upon further investigation, have acted to increase my understanding of rarefied flows. To my readers, Steven Senturia and Howard Stone thank you for the editing comments on the later drafts.

In the area of analysis, Issac Greber has always been a willing and eager participant. Without question, my understanding of the models presented in this thesis (and their limitations) has been significantly impacted by Issac's inquiries.

In terms of providing me with data, John Harley was kind enough to rummage through his work at the University of Pennsylvania (after having finished and moved on) and this, in my opinion, goes way beyond the "call of duty". Chi-Ming Ho from UCLA also provided me access to the raw data from their work on microchannel flow which I appreciate.

In the area of general fabrication and instrumentation, Don Weiner and Dick Perdichizzi of the Aero/Astro machine shop and student laboratory have been been supportive throughout. In the area of microfabrication, the entire MTL staff of research specialists and laboratory technicians have been extremely supportive and helpful. However, the help (as I worked my way through the microfabrication) of Paul Tierney, Tim Tyson, Brian Foley as well as Octavio Hurtado (now retired) stand out in my mind.

In terms of my understanding of specific MEMS processing, foremost among the contributions of many of the recent graduate students who have made or are making their way through MTL has been Lalitha Parameswaran's. Lalitha has always been a willing listener, a kind instructor and good friend. Of course during my time at MIT, I have made many good friends and their "contributions" have primarily come in the form of coffee or beer. Of note, Ruben Rathnasingham and Ravi Srinivasan have always been willing contributors... especially in the latter-mentioned form.

I also thank the many graduate students and post-docs that I have had the pleasure of working with over the last several years for making my time at MIT memorable and deeply rewarding. These people include Charles Hsu, Aravind Padmanabhan, Vince McNeil, Howard Goldberg, John Gilbert, Ed Piekos, DJ Orr, Beth Grimaldi, Mark Sheplak, CC Lin, Albert Folch, Samara Firebaugh, Joey Wong, Roberto Devoto and Joel Voldman.

I acknowledge all of the various support provided me by my family. To my brothers and sister for their love and friendship, to my parents for their love and encouragement, thank you all. Finally, of *all* the contributions, my wife's stands out as the most meaningful. Her understanding and steadfast love have always been a source of profound tranquility during this sometimes hectic journey. Thank you Kerri.

"Would you tell me, please which way I ought to go from here?" asked Alice.
"That depends a good deal on where you want to get to," said the Chesire Cat.

-Lewis Carroll, *Alice's Adventures in Wonderland*

Contents

List of Figures

Chapter 1

Introduction

Because the surface area to volume ratio of MicroElectroMechanical Systems (MEMS) can be large, $\mathcal{O}(10^6)$m, dynamic properties which are related to surface phenomena often dominate system performance [1], [2]. For example, due to the momentum exchanged between the proof mass and air gap, the typical dynamic response of a micromachined accelerometer operated at atmospheric conditions is often over-damped. To overcome the performance limitations associated with this damping, researchers have suggested a number of approaches from operating these micromachined systems in vacuum to mitigating the damping by clever mechanical design [3], [4]. However, regardless of the approach taken to enhance the performance of these systems, a clear understanding of and ability to accurately model the exchange of momentum which occurs at the interface of MEMS and the surrounding fluid is essential.

Because of the unique attribute associated with the scale of MEMS, to understand and effectively model the exchange of momentum between these systems and their fluid surroundings requires an understanding of the limitations of some of the underlying assumptions which are commonly employed in the study of fluid dynamics. Among these assumptions is that of no-slip at the fluid-solid interface. No-slip at the fluid-solid interface is the standard boundary condition which is assumed throughout the vast majority of the flow fields encountered in the study of fluid dynamics and this boundary condition states simply that the streamwise velocity at the fluid-solid interface goes to the the velocity of the interface. However, because the relevant lengths scales of MEMS are on the order of microns and MEMS are often operated in gaseous environments at standard conditions, where the molecular mean free path is approximately 70 nm, the dynamics of MEMS can easily exhibit rarefied behavior. Under these conditions, the assumption of no-slip at the boundary ceases to adequately describe the exchange of momentum which occurs at the fluid-solid interface and an analysis which employs this boundary condition does not accurately describe the fluid dynamics.

The boundary condition at the interface is dependent on the properties of the flow and the extent to which the surrounding fluid accommodates to the state of the surface; for the conditions encountered in today's MEMS, it is the slip-flow boundary condition. The properties of the flow which are relevant to the slip-flow boundary condition include the mean free path, the gradient of the flow velocity near the fluid-solid interface and the fractional momentum exchange between the fluid and the surface, which is parameterized in a coefficient known as the Tangential Momentum Accommodation Coefficient (TMAC). For many fluid-solid interfaces, the TMAC is near unity. However, it has not been characterized for surfaces and conditions present in MEMS. The goal of this thesis is to develop a means by which the TMAC can be measured for various MEMS surfaces and to measure values of the TMAC for one type of surface which is common in MEMS, a single-crystal prime-silicon surface upon which a native oxide resides. Furthermore, we would like to make these measurements over a range of characteristic flow conditions which would be encountered in state-of-the-art MEMS.

To achieve these goals, we have developed an experimental regimen which utilizes our knowledge of canonical two-dimensional channel flow to extract values of the TMAC from pressure drop and mass flow measurements made on a micromachined channel. We have developed a simple and robust fabrication technique for making high-integrity channels, we have derived analytical models which are conducive to the measurement of the TMAC and we have developed a unique means for making high-resolution mass flow measurements.

1.1 Significance of the Knudsen Number

The study of flow in small channels for the purposes of elucidating rarefied phenomena is not new. In 1909 Knudsen published a paper in which he explained theoretically and demonstrated experimentally the effects of rarefied flow in capillaries at low pressure. He undertook a series of flow experiments on glass capillaries, the smallest of which was 66 microns in diameter and the largest 282 microns [5]. In this seminal work, Knudsen studied flow regimes from continuum to free molecular flow and introduced the significance of the ratio of mean free path to characteristic dimension, now known as the Knudsen number (K) [5]. The Knudsen number is defined as:

$$K = \frac{\lambda}{H}, \tag{1.1}$$

where, λ is the mean free path and H is the flow characteristic dimension. For an ideal gas modeled as rigid spheres, a simple expression can be derived for the mean free path [6]:

$$\lambda = \frac{\kappa T}{P\sigma^2\pi\sqrt{2}}, \tag{1.2}$$

where κ is the Boltzmann constant, T is the temperature, P is the pressure, and σ is the molecular diameter.

Like the Reynolds and Mach numbers, the Knudsen number can be used for flow regime characterization and there are four flow regimes based on the order of the Knudsen number. They are continuum flow, slip flow, transition flow and free molecular flow. The classical demarcation of the regimes is given below [7].

If $K < 0.01$, the flow is said to be in the continuum-flow regime.

If $0.01 < K < 0.1$, the flow is said to be in the slip-flow regime.

If $0.1 < K < 3$, the flow is said to be in the transition-flow regime.

If $3 < K$, the flow is said to be in the free molecular regime.

Knudsen empirically demonstrated that, when $K \gg 1$, the flow in long cylindrical tubes can be modeled with kinetic theory. In the slip-flow and continuum regimes, he showed that the Navier-Stokes equations with a boundary condition of velocity slip could model the flow (in the limit of continuum flow, the slip boundary condition goes to zero). Adequate models for the transition regime were and continue to be elusive. In addition to the empirical evidence of the significance of the Knudsen number for characterizing the flow regime, there is qualitative evidence based on theory.

It is generally accepted that the governing equation for all flow regimes is the Boltzmann equation, which describes the time rate of change of the distribution function due to molecular motion [8]. While it is believed that this equation represents flow properties under all known conditions, the complexity of this equation prohibits a direct solution and approximations must be made. For example, in the case in which the flow is not far from equilibrium (Knudsen number less than unity), the Chapman-Enskog expansion can be used to approximate the Boltzmann equation. By undertaking an asymptotic perturbation expansion (in Knudsen number) around the equilibrium Maxwellian distribution, the Boltzmann equation can be shown to reduce to sets of more familiar expressions. For instance, in the the case of an ideal gas in which molecules are modeled as rigid spheres, the zeroth-order approximation based on the Chapman-Enskog expansion of the Boltzmann equation gives the inviscid Euler equations, the first-order approximation gives the Navier-Stokes equations (accurate to $\mathcal{O}(K)$) and the second-order approximation gives the Burnett equations (accurate to $\mathcal{O}(K^2)$). This analysis of the Boltzmann equation based on the Chapman-Enskog expansion is the basis for the qualitative evidence of the significance of the Knudsen number in determining flow regimes. For viscous flow, in the case of small Knudsen number, the Navier-Stokes equations are adequate for describing the flow (continuum and slip-flow regime). As the Knudsen number increases, the higher-order terms of the Burnett equations become significant and the Navier-Stokes equations fail (transition regime). Eventually, as the Knudsen number continues to increase, the initial assumption of the Chapman-Enskog expansion, which is that the flow is not far from equilibrium, fails and the flow enters the free molecular regime.

In cases where viscous stress is an integral aspect of the flow dynamics, we have two sets of equations with which to model the flow dynamics: The Navier-Stokes equations (accurate to $\mathcal{O}(K)$) and the Burnett equations (accurate to $\mathcal{O}(K^2)$). However, the complexity of the formulation of the viscous stresses (momentum conservation) and heat fluxes (energy conservation) typically preclude the application of the Burnett equations and so, for most cases, we employ the Navier-Stokes equations. In addition to the complexity of

the formulation of the stress and flux terms, the Burnett equations require ill-defined boundary conditions and, under certain situations, have been shown to violate the second law of thermodynamics [9]. Due to these difficulties, before we attempt system modeling based on the Burnnett equations, the limitations of the Navier-Stokes equations should be well-established.

In the case of MEMS, researchers have typically utilized the Navier-Stokes equations for modeling. The standard boundary condition of no-slip is normally invoked and the analysis is carried through as if no rarefaction were present [1], [10], [11]. In fact, the no-slip or non-rarefied approach is valid for many MEMS in which the characteristic dimensions are on the order of several tens of microns and the systems are operated at atmospheric pressure where the mean free path is approximately 70 nm. For instance, for the case of an accelerometer operated in a standard atmosphere, it has been suggested that the height above the substrate at which the proof mass is suspended (air gap) H must be significantly greater than 10 microns if rarefaction effects are to be ignored [10]. If $H = 20$ μm and the mean free path is approximately 70 nm, the Knudsen number is approximately 0.004 which is characteristic of the continuum regime. Therefore, an analysis based on the Navier-Stokes equations with the no-slip boundary condition should be valid for such a system. However, as the dimensions of MEMS operated at atmospheric pressure decrease or as MEMS are increasingly operated in low-pressure regimes where the mean free path increases, the validity of this approach will falter. For instance, there currently exist structures where the characteristic dimension is on the order of microns. For example see references [12], [13], [14], [15]. If such devices are operated at standard conditions, then K is $\mathcal{O}(10^{-2})$ and the structures are being operated in the slip-flow regime.

If, as suggested by the Knudsen number, the Navier-Stokes equations with no-slip boundary conditions are no longer valid for these MEMS, then the question is: is it possible to extend the Navier-Stokes analysis for MEMS by introducing new boundary conditions? That is, do the slip-flow solutions of the Navier-Stokes equation adequately model the momentum exchange between MEMS and the fluids in which they are immersed? To answer this question, researchers have conducted flow studies on micromachined channels [16] [17] and have found that, in order to adequately model the pressure drop-mass flow data, the boundary conditions on the Navier-Stokes equations have to include the presence of wall slip.

1.2 Wall-Slip

The presence of wall-slip was first proposed in the last century by Kundt and Warburg [18]. In their studies, they found that, with a decrease in pressure, the decay of the amplitude of an oscillating disk which was suspended inside of a vacuum by a quartz fiber became slower than that which could be attributed to typical viscous drag. Based on these findings, Kundt and Warburg, proposed that the decrease in viscous damping was not a result of a pressure dependence of viscosity, but rather the result of incomplete interaction between the gas and the surface of the disk [18]. They proposed that it was the velocity gradient and not the viscosity which was functionally dependent on pressure and this dependence resulted in a decrease in the shear stress (decrease in the damping of the oscillations).

Later Maxwell [19] proved, on the basis of Kinetic Theory, the existence of wall slip. He showed, that, in the presence of zero wall-normal temperature gradient ($dT/dy = 0$), the velocity near a wall in shear flow could be shown to be:

$$u_w = \frac{2-f}{f}\lambda \left.\frac{du}{dy}\right|_w + \frac{3}{4}\frac{\mu}{\rho T}\left.\frac{dT}{dx}\right|_w, \tag{1.3}$$

where λ is the mean free path, u is the streamwise velocity, y is the wall-normal direction, x is the streamwise direction, μ is the bulk viscosity, ρ is the density and T is the temperature. Maxwell introduced the coefficient f to account for the percentage of streamwise momentum that molecules transfer upon a collision.

Expression (1.3) is commonly referred to as the first-order correction for wall slip and it should be noted that second-order slip-flow expressions have been derived as well as series expansions for the case of zero thermal gradients, i.e., [20]:

$$u_w = \frac{2-f}{f}\left[\lambda \left.\frac{du}{dy}\right|_w + \frac{\lambda^2}{2}\left.\frac{d^2u}{dy^2}\right|_w + \frac{\lambda^3}{6}\left.\frac{d^3u}{dy^3}\right|_w + \cdots\right]$$

Though these expressions have been derived, the applicability of these higher-order boundary conditions to the Navier Stokes equations is questionable because the Navier-Stokes equations are only accurate to $\mathcal{O}(K)$.

For the case of no streamwise thermal gradient $dT/dx = 0$, equation (1.3) can be non-dimensionalized by a characteristic dimension and velocity to obtain [21]:

$$\tilde{u}_w = \frac{2-f}{f} K \left. \frac{d\tilde{u}}{d\tilde{y}} \right|_w , \tag{1.4}$$

where the tilde ($\tilde{}$) represents non-dimensional quantities and K is the Knudsen number. This expression clearly shows that there exists a non-zero velocity at the wall and that the magnitude of both the Knudsen number and the coefficient f govern the extent of the slip.

1.2.1 The Tangential Momentum Accommodation Coefficient

Maxwell postulated that when molecules strike a surface some percentage of them rebound from the surface without transferring any of their streamwise momentum, others transfer all of their momentum and the ratio of the number of molecules rebounding without any streamwise momentum exchange to those that transfer all of their momentum is a physical characteristic based on surface and gas properties. In order to capture this effect in his analysis, the results of which are given above, Maxwell introduced the coefficient f. Like Maxwell, Knudsen recognized that the mode of scattering of gas molecules from surfaces was a fundamental aspect of his analysis [5]. He stated (and found empirically) that, under free molecular conditions, diffuse reflection was the most likely model for gas-surface interactions. The implication of diffuse reflections is that, on average, each molecule which hits a wall transports all of its momentum to the wall upon impact i.e., upon impact all information about pre-collision streamwise momentum is lost. This concept of molecular reflection first introduced by Maxwell and later discussed by Knudsen can be expressed as a function of incident and reflected momentum. That is, for a single gas species, the ratio that relates the amount of streamwise momentum which is transferred to the wall upon collision is:

$$\frac{u_r - u_i}{U_w - u_i} = \sigma_m , \tag{1.5}$$

where u_r is the average reflected streamwise velocity, u_i is the average incident streamwise velocity and U_w is the streamwise velocity of the surface. The ratio given by equation (1.5) is known as the Tangential Momentum Accommodation Coefficient (TMAC) and has a slightly different meaning than Maxwell's f but an identical impact on the analysis. Diffuse reflections, like those postulated by Knudsen, are a result of complete momentum accommodation, $\sigma_m = 1$, and for most engineering surfaces $\sigma_m \approx 1$ as Knudsen proposed. However, under controlled test conditions, values of σ_m less than unity have been reported [22], [23], [24].

The effects of gas-surface properties and surface treatment have been shown to play a crucial role in determining the size of the TMAC [23] [24]. For example, Seidl and Steinheil [24] have studied helium molecular beam scattering from various crystal, polycrystalline and amorphous materials and have found that the TMAC strongly depends on the material and surface state and that the TMAC can be reduced by applying suitable surface preparation techniques. Using molecular beams they measured the TMAC as a function of angle of incidence and have found that, for a given angle of incidence, different materials covered with similar adsorbates (mainly hydrocarbons and water) possess different TMACs. For polished sapphire, they reported $\sigma_m \approx 0.7$. They also report that, for an epitaxially grown layer of gold $<111>$, partially removing the adsorbed material can significantly reduce the TMAC from values near unity to values as low as 0.2. In this work, no quantitative data about the specimen surface roughness were reported. However, they do demonstrate that, even for adsorbate contaminated surfaces, the bulk material properties play a crucial role in determining the TMAC and we believe that the surface roughness is one such property.

As another example, in 1974, Thomas and Lord [23] reported on a series of experiments conducted in a low pressure apparatus in part to determine the TMAC for controlled surfaces. In this work, the drag on magnetically suspended steel spheres with various surface treatment was measured, and the TMAC was derived from these measurements. They measured the drag on two sets of 0.635 cm steel spheres. One set was polished and possessed a mirror-smooth surface with an rms surfaces roughness of 0.1 μm and the other set was intentionally roughened to remove the mirror smooth finish. The spheres were then loaded into the vacuum system and baked in-situ at 400 °C for several hours. They reported values for the TMAC for the roughened balls slightly above unity for the gases helium, neon, argon and xenon and offer as a possible

explanation of greater than unity TMAC the effect of net back scattering. For the smooth balls, values of the TMACs were dependent on the gas and ranged from 0.824 to 0.943, with the smaller, lighter gases producing the lower values.

These investigations have demonstrated that, under controlled test conditions, values of the tangential momentum accommodation coefficients for various surfaces less than unity can exist. However, for the case of Seidl and Steiheil [24], the studies were of monoenergetic molecular beams impinging on surfaces, and in the case of Thomas and Lord, the study was carried out in the presence of a low-density gas. For the case of MEMS, the impinging gas will not be monoenergetic beam, with a unidirectional component and the gas density will be at or near atmospheric conditions. Therefore, due to the varied experimental approaches and materials, the results of these previous studies on the TMAC can not be directly applied in a quantitative manner to MEMS.

Still, there have been studies on internal flow in small dimensional channels that have reported TMACs of less than unity. For instance, Porodnov *et al.* [25] have shown that by coating 90 μm glass channels with oil, they could reduce the TMAC from near unity to values as low as 0.895. Recently, a study was undertaken to determine the effect that adsorbed oxygen had upon the tangential momentum accommodation coefficient of a titanium coated tube which was 9.3 mm in diameter [26]. It was found that, for helium, the TMAC could be reduced from near unity (0.93) to 0.65 by removing the adsorbed oxygen from the surface. No surface roughness data were reported.

These studies amply demonstrate that values for the tangential momentum accommodation coefficient of less than unity can and do exist. Furthermore, they suggest that the surface material and gas species, as well as the surface condition, and perhaps the gas condition play a significant role in determining the TMAC. However, there currently does not exist a theory which we are aware of that can be used to predict the TMAC for a given surface condition. Yet the value of the TMAC definitely plays a fundamental role in determining the boundary condition which exists at the gas-surface interface and, as in the case of MEMS, the value of the TMAC for characteristic gas-surface systems remains unknown. Therefore, we believe that a systematic study of one such surface commonly present in MEMS will represent a significant contribution to the advancement of fluid modeling for MEMS.

Because it is currently impossible to make a direct measurement of the tangential momentum accommodation coefficient at the pressures of interest (near atmospheric), the value of the TMAC must be inferred by other means. In the approach taken in this thesis, we use the canonical channel flow and our understanding of slip phenomena to extract values of the TMAC from experimental measurements and a theoretical model.

1.3 Microchannel Flow

Rarefied flow in channels has been extensively studied by researchers in the rarefied gas community. For a good discussion of the significant contributions through the year 1977 see Edwards [27]. The work conducted by this community was driven by low-density applications of vacuum and orbital sciences where it was the mean free path that approached the macroscopic length scales of the vacuum or space-based system. Recently the advancements in micromachining have opened a new area where rarefied gas behavior becomes relevant, namely when the microscopic dimension of the system approaches that of the gas mean free path. Due to the fact that this rarefaction occurs at near-atmospheric pressure, it has been suggested that many of the rarefaction phenomena which have been typically thought of as laboratory curiosities could have a significant impact on these microfabricated devices [28]. To investigate the impact of atmospheric rarefaction on MEMS previous studies of gaseous flow in micromachined channels have been conducted by Harley *et al.* [16], Arkilic *et al.* [29], Pong *et al.* [30], Beskok and Karniadakis [20] and Piekos and Breuer [31]. Also, studies of a compressible fluid in microgeometries, *without* the incorporation of rarefied behavior have been conducted recently by Prud'homme *et al.* [32] and van den Berg *et al.* [33].

The work of Prud'homme *et al.* [32] is a perturbation solution of the Navier-Stokes equations for radially symmetric geometries with the assumption of no radial pressure gradient. Although the one-dimensional model presented in their work does not include rarefaction effects, it does show the significance of gas compressibility upon the pressure distribution i.e., the existence of non-constant pressure gradients. The work of van den Berg *et al.* [33] is also a one-dimensional perturbation analysis of radially symmetric flow without the incorporation of rarefied effects. This work was undertaken in an attempt to analyze a rigorous

method by which one could characterize gaseous viscosity with a capillary flow viscometer. The existence of non-constant pressure gradients and the contribution of compressibility was shown and it was demonstrated that a capillary viscometer, based on the one-dimensional Navier-Stokes equations, gave viscosity results comparable to the accepted values.

Gaseous flow in two-dimensional micromachined channels with a Cartesian geometry for various Knudsen numbers was studied by Harley *et al.* [16]. This investigation included analytic and experimental work on rarefied microchannel flow. The model used for rarefied flow assumed negligible wall-normal pressure gradients and was based on the streamwise momentum equation of the Navier-Stokes equations, with the non-linear terms neglected. The continuity equation was satisfied in an integral form and the boundary condition for the solution consisted of the first-order correction of the non-zero wall velocity commonly used for slightly rarefied flow. This study demonstrated the existence of non-zero wall velocity in microchannels and showed the contribution of the non-zero slip on the mass flow-pressure drop relationship. However, the fabricated channels did not possess well controlled surface structure (the channel was made by the bonding of silicon and glass) and the technique used to characterize the mass flow was susceptible to thermal fluctuations. Previous work of Arkilic *et al.* [29] on two-dimensional gaseous microchannel flow showed analytically the effects of wall-slip on the pressure gradient and, by analysis and experiment, the mass flow-pressure drop relationship for channels with uniform surface structure. In this work, nonlinear terms were ignored and the streamwise and wall-normal momentum as well as the *differential* continuity equations were satisfied. The previous work of Pong *et al.* [30] was an experimental investigation into the pressure distribution that exists in microchannel flow. By conducting on-chip pressure measurement of microchannel flow, they have shown empirically that compressibility is an important feature in a microchannel. Recently, the work of Shih *et al.* which is an extension of the work of Pong *et al.* have reported mass flow measurements in these channels [34].

In addition to the analytic and/or experimental investigations, there has also been work on the simulation of rarefied gas behavior of microchannel flow. Beskok and Karniadakis [20] have presented numerical solutions of the Navier-Stokes and energy equations for flows with slight rarefaction i.e., slip-flows, and they have shown that the mass flow within a channel may be increased by both slip and thermal-creep effects. Piekos and Breuer [31] have made use of the Direct Simulation Monte Carlo (DSMC) method for simulations of channels and, unlike previous analytic and computational investigations, where the results were based on the Navier-Stokes equations, the DSMC approach is valid for the full range of flow regimes (continuum through free molecular). In the slip-flow regime, the DSMC results of Piekos and Breuer are in good agreement with the analytic model and experimental data previously presented [29]

The analysis presented in this thesis is differentiated from our previous microchannel studies by the fact that expressions which can be used to easily extract the TMAC are derived. In addition, we present an analytic framework which can be used for theory validation.

1.4 Thesis Structure

The structure of this thesis is as follows. In Chapter 2 we develop a non-dimensionalization of the slip-flow governing equations for flow in a micromachined channel. We solve the system of equations for the unknowns in the flow including streamwise and wall-normal velocities as well as pressure. We also derive expressions which can be used to extract values for the TMAC from pressure and high-resolution mass flow measurements on micromachined channels. In Chapter 3, a description of the channel fabrication is presented. Chapter 4 introduces the mass flow hardware and test procedure. It begins with a discussion of low-flow primary standards and moves on to the problems associated with making low-flow measurements at the pressures near atmospheric and how these problems are addressed. In Chapter 5, the flow data are presented and concluding remarks are made in Chapter 6.

Chapter 2

Analytic Results

2.1 Governing Equations

We consider a two-dimensional flow, neglecting variations in the z-direction. This is valid for channels of high aspect ratio, and it is easy to show that the error is only proportional to the inverse square of the aspect ratio [35]. The geometry for our solution is shown in figure 2.1 and the full two-dimensional time-invariant Navier-Stokes equations for a compressible fluid, ignoring body forces are (in Cartesian coordinates):

$$\rho\left(u\frac{\partial u}{\partial x}+v\frac{\partial u}{\partial y}\right) = -\frac{\partial p}{\partial x}+\mu\left(\frac{\partial^2 u}{\partial x^2}+\frac{\partial^2 u}{\partial y^2}+\frac{1}{3}\left(\frac{\partial^2 u}{\partial x^2}+\frac{\partial^2 v}{\partial x\partial y}\right)\right) \tag{2.1}$$

$$\rho\left(u\frac{\partial v}{\partial x}+v\frac{\partial v}{\partial y}\right) = -\frac{\partial p}{\partial y}+\mu\left(\frac{\partial^2 v}{\partial x^2}+\frac{\partial^2 v}{\partial y^2}+\frac{1}{3}\left(\frac{\partial^2 v}{\partial y^2}+\frac{\partial^2 u}{\partial x\partial y}\right)\right). \tag{2.2}$$

The continuity equation is given by

$$\nabla.(\rho\vec{u})=0, \tag{2.3}$$

while the equation of state for an ideal gas is given by

$$p=\rho\mathcal{R}T. \tag{2.4}$$

Here, u and v are the streamwise and wall-normal components of velocity $\vec{u}$, μ is the molecular viscosity, ρ is the density and $\mathcal{R}$ is the specific gas constant. In the momentum equations, we have assumed a Stokes hypothesis for the second coefficient of viscosity [35], although it will be shown in equations (2.13) & (2.16) that these terms do not enter the analysis to lowest order. We choose a non-dimensionalization of the variables in the following manner: velocities (u,v) are normalized by the area-averaged streamwise velocity at the channel exit $(\bar{u})$; the streamwise coordinate, x by the channel length, L; the wall-normal coordinate, y, by the channel height, H; and lastly density, ρ, and pressure, p, by the channel outlet conditions, $\bar{\rho}$ and $\bar{p}$. A further simplification is that of isothermal flow. This is a good assumption for low Mach number flows ($M \ll 1/\sqrt{\gamma}$) in long uninsulated channels, which is certainly the case for data presented by Harley *et al.* [16], Pong *et al.* [30] and the data subsequently presented here. With these assumptions, the momentum equations can be recast into non-dimensional form:

$$R\tilde{p}\left(\epsilon\tilde{u}\frac{\partial\tilde{u}}{\partial\tilde{x}}+\tilde{v}\frac{\partial\tilde{u}}{\partial\tilde{y}}\right) = -\frac{\epsilon R}{\gamma M^2}\frac{\partial\tilde{p}}{\partial\tilde{x}}+\epsilon^2\frac{\partial^2\tilde{u}}{\partial\tilde{x}^2}+\frac{\partial^2\tilde{u}}{\partial\tilde{y}^2}+\frac{1}{3}\left(\epsilon^2\frac{\partial^2\tilde{u}}{\partial\tilde{x}^2}+\epsilon\frac{\partial^2\tilde{v}}{\partial\tilde{x}\partial\tilde{y}}\right) \tag{2.5}$$

$$R\tilde{p}\left(\epsilon\tilde{u}\frac{\partial\tilde{v}}{\partial\tilde{x}}+\tilde{v}\frac{\partial\tilde{v}}{\partial\tilde{y}}\right) = -\frac{R}{\gamma M^2}\frac{\partial\tilde{p}}{\partial\tilde{y}}+\epsilon^2\frac{\partial^2\tilde{v}}{\partial\tilde{x}^2}+\frac{\partial^2\tilde{v}}{\partial\tilde{y}^2}+\frac{1}{3}\left(\frac{\partial^2\tilde{v}}{\partial\tilde{y}^2}+\epsilon\frac{\partial^2\tilde{u}}{\partial\tilde{x}\partial\tilde{y}}\right), \tag{2.6}$$

where $R=\bar{\rho}\bar{u}H/\mu$, is the Reynolds number which is constant in x and evaluated at the outlet conditions, and M is the outlet Mach number based on $\bar{u}$ (derived using $c^2=\gamma\mathcal{R}T$), all the other terms are non-dimensionalized as described above and the non-dimensional form is represented by $(\tilde{})$. We have also used

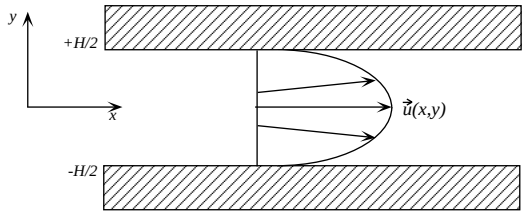

Figure 2.1: Geometry for channel analysis, with a flow profile at a given position. The wall-normal components of the velocity vector are exaggerated.

the equation of state for an isothermal flow which allows us to replace density by pressure throughout. Lastly, ϵ is the ratio of the channel height to its length:

$$\epsilon = \frac{H}{L} \tag{2.7}$$

and is considered to be small.

The non-dimensional continuity equation can be written as:

$$\epsilon \frac{\partial(\tilde{p}\tilde{u})}{\partial \tilde{x}} + \frac{\partial(\tilde{p}\tilde{v})}{\partial \tilde{y}} = 0. \tag{2.8}$$

2.1.1 Boundary Conditions

The boundary conditions are that the vertical velocity, $\tilde{v}$, vanishes at the solid wall and that the streamwise velocity at the wall, $\tilde{u}$ is given by equation (1.3), repeated here for convenience:

$$\tilde{u}|_{wall} = \frac{2-\sigma_m}{\sigma_m} K \left.\frac{\partial \tilde{u}}{\partial \tilde{y}}\right|_{wall}, \tag{2.9}$$

where σ_m is the unknown tangential momentum accommodation coefficient which replaces Maxwell's f. Rigorously, for the geometry here, the wall velocity given by equation (2.9) is for $-H/2$. At $+H/2$ where $\left.\frac{\partial \bar{u}}{\partial \bar{y}}\right|_{wall}$ is *negative*, the wall velocity is given by the negative of equation (2.9).

2.2 Analysis

We now expand $\tilde{u}, \tilde{v}$ and $\tilde{p}$ in powers of ϵ:

$$\tilde{u} = \tilde{u}_o + \epsilon\tilde{u}_1 + \epsilon^2\tilde{u}_2 + \ldots \tag{2.10}$$

$$\tilde{v} = \tilde{v}_o + \epsilon\tilde{v}_1 + \epsilon^2\tilde{v}_2 + \ldots \tag{2.11}$$

$$\tilde{p} = \tilde{p}_o + \epsilon\tilde{p}_1 + \epsilon^2\tilde{p}_2 + \ldots \tag{2.12}$$

and substitute into the equations above. Two non-dimensional parameters, R and M, which appear in the non-dimensional governing equations determine the flow regime and, within the context of the perturbation expansion, they can independently have three values: $\mathcal{O}(\epsilon)$, $\mathcal{O}(1)$ or $\mathcal{O}(1/\epsilon)$, leading to nine independent flow regimes.

In this study, we consider $M = \mathcal{O}(\epsilon)$ and $R = \mathcal{O}(\epsilon)$. Thus, $R/M^2 = \mathcal{O}(1/\epsilon)$ from which we immediately see from the y-momentum equation that at $\mathcal{O}(1/\epsilon)$,

$$\tilde{p}_o = \tilde{p}_o(\tilde{x}). \tag{2.13}$$

The continuity equation, evaluated at lowest order, $\mathcal{O}(1)$, results in:

$$\tilde{p}_o(\tilde{x})\tilde{v}_o(\tilde{x},\tilde{y}) = f(\tilde{x}). \tag{2.14}$$

Evaluating this at the wall ($\tilde{y} = \pm 1/2$), and realizing that $\tilde{p}_o$ can not be uniformly zero for all $\tilde{x}$, we conclude that

$$\tilde{v}_o = 0. \tag{2.15}$$

Using these results, the $\tilde{x}$-momentum equation, at $\mathcal{O}(1)$, may be written as

$$\frac{\epsilon R}{\gamma M^2} \frac{d\tilde{p}_o}{d\tilde{x}} = \frac{\partial^2 \tilde{u}_o}{\partial \tilde{y}^2}. \tag{2.16}$$

This set of equations is similar to what one would obtain for a "normal" channel flow i.e., one in which variation in the streamwise direction is assumed to be negligible. However, in this model, the streamwise velocity is dependent upon the wall-normal ($\tilde{y}$) *and* streamwise ($\tilde{x}$) direction. This essential difference is due to the fact that the present analysis, unlike a conventional analysis, makes no assumptions about the variation of the wall-normal component of velocity or streamwise variation of the pressure gradient.

Utilizing symmetry conditions and the slip-flow boundary condition (2.9), the $\tilde{x}$-momentum equation (2.16) can be integrated twice with respect to $\tilde{y}$ to obtain:

$$\tilde{u}_o(\tilde{x}, \tilde{y}) = -\frac{\epsilon R}{8\gamma M^2} \frac{d\tilde{p}_o}{d\tilde{x}} \left(1 - 4\tilde{y}^2 + 4 \frac{2 - \sigma_m}{\sigma_m} K \right), \tag{2.17}$$

where K denotes the *local* Knudsen number (based on channel height) and is inversely proportional to $\tilde{p}_o$.

Substituting this into the continuity equation at order $\mathcal{O}(\epsilon)$, and integrating once in $\tilde{y}$, we can derive an equation for $\tilde{v}_1(\tilde{x}, \tilde{y})$:

$$\tilde{v}_1 = \frac{\epsilon R}{8\gamma M^2} \frac{1}{\tilde{p}_o} \left[\frac{1}{2} \frac{d^2(\tilde{p}_o^2)}{d\tilde{x}^2} \left(\tilde{y} - \frac{4}{3}\tilde{y}^3 \right) + 4 \frac{2 - \sigma_m}{\sigma_m} K_o \tilde{y} \frac{d^2 \tilde{p}_o}{d\tilde{x}^2} \right], \tag{2.18}$$

where K_o is Knudsen number evaluated at the outlet. The subscript o is used here to denote the *outlet* conditions and is unrelated to the *order* of the Knudsen number.

Evaluating this at the wall, where the wall-normal velocity must vanish, results in a solvability condition:

$$\frac{d^2(\tilde{p}_o^2)}{d\tilde{x}^2} + 12 \frac{2 - \sigma_m}{\sigma_m} K_o \frac{d^2 \tilde{p}_o}{d\tilde{x}^2} = 0. \tag{2.19}$$

Satisfying this equation will automatically satisfy the boundary condition on $\tilde{v}_1$ at both walls. The solution to this equation is straightforward and using the fact that $\tilde{p}_o = 1$ at the outlet ($\tilde{x} = 1$) we find an expression for the zeroth-order pressure distribution:

$$\tilde{p}_o(\tilde{x}) = -6 \frac{2 - \sigma_m}{\sigma_m} K_o + \sqrt{(6 \frac{2 - \sigma_m}{\sigma_m} K_o)^2 + (1 + 12 \frac{2 - \sigma_m}{\sigma_m} K_o)\tilde{x} + (\mathcal{P}^2 + 12 \frac{2 - \sigma_m}{\sigma_m} K_o \mathcal{P})(1 - \tilde{x})}, \tag{2.20}$$

where $\mathcal{P}$ is the inlet to outlet pressure ratio.

The solutions obtained are correct to zeroth order ($\tilde{v}$, to $\mathcal{O}(\epsilon)$) and indicate a parabolic streamwise velocity profile which changes slowly down the length of the channel as the pressure drops. The expansion appears to be well-ordered and the next order equations could be solved to yield higher-order corrections to $\tilde{u}, \tilde{v}$ and $\tilde{p}$. However, the accuracy of the high-order terms may be limited by the basic two-dimensional assumption.

The predicted pressure distribution, $\tilde{p}_o(\tilde{x})$, is shown in figure 2.2 for a long channel with a pressure ratio of 2.7 and σ_m assumed equal to unity. Three cases are shown: a linear distribution with no rarefaction, one with compressibility and outlet Knudsen number of zero (no rarefaction) and one with an outlet Knudsen number of 0.059, corresponding to a channel with height 1.3 microns charged with nitrogen and exhausting to atmospheric conditions. This particular case corresponds to one of the conditions reported by Pong *et al.* [30], whose data are also plotted for comparison. There are several features of this figure to notice. One immediately sees that, by including compressibility, the predicted pressure distribution for both Knudsen

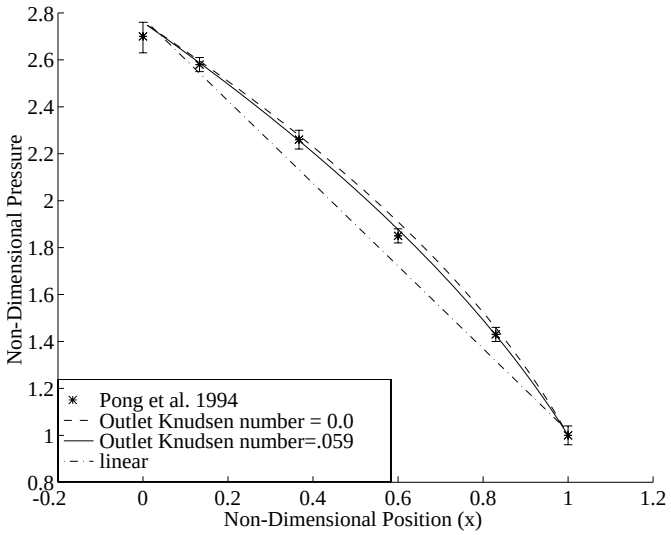

Figure 2.2: Pressure distribution in a long microchannel. The dashed curve represents the pressure for a flow with no rarefaction (equation (2.20) with $K_o = 0$) while the solid curve represents the pressure for a flow with an outlet Knudsen number of 0.059. The dotted line is a straight-line pressure drop that would be predicted using a constant-density analysis. The symbols are the data from Pong *et al.*, plotted for comparison.

number regimes is nonlinear, with negative curvature. This nonlinearity is due to the change in density of the gas in the long channel and one sees that the effect of moderate Knudsen number is actually to diminish this curvature. The experimental data fit quite well, and the uncertainty in the data reported by Pong *et al.* [30] exceeds the mismatch between their measurements and the current predictions. We should note that the "second generation" data reported by Pong *et al.* [30] do *not* fit this curve very well and the discrepancy is an issue still to be resolved.

Having solved for the pressure distribution, we now have a complete expression for the streamwise and normal velocity components and the mass flow distribution. These are shown in figures 2.3, 2.4 and 2.5 with σ_m assumed equal to unity. Note that the slip velocity at the wall (figure 2.4) increases markedly toward the exit as the pressure begins to drop faster. To enforce mass continuity, mass must migrate from the channel centerline towards the wall. This is reflected in the mass flow contours (figure 2.5) which show a drift of mass towards the wall as the flow progresses down the channel. This mass migration will affect molecules of varying masses differently, raising the possibility of constructing a microscale system for gas-separation. It is worth noting that, if $K_o = 0$, the pressure distribution simplifies (it is still nonlinear due to the change in density along the channel) such that $d^2(\tilde{p}^2)/d\tilde{x}^2 = 0$. Therefore by equation (2.18), when $K_o = 0$, the wall-normal velocity goes to zero suggesting that, for the incompressible model presented here, the wall-normal velocity is solely a function of rarefaction.

2.2.1 Mass Flow Expression

We can calculate the mass flow through the channel for given inlet and outlet pressures, by multiplying the expression for $\tilde{u}(\tilde{y})$ (2.17) by the density and integrating across the channel and evaluating at $\tilde{x} = 1$. Doing this, the *dimensional* mass flow is given by:

$$\dot{m} = \frac{H^3 w P_o^2}{24 \mu L \mathcal{R} T} (\mathcal{P}^2 - 1 + 12 \frac{2 - \sigma_m}{\sigma_m} K_o (\mathcal{P} - 1)), \tag{2.21}$$

where P_o is the (dimensional) outlet pressure, w is the channel width and $\mathcal{P}$ is the inlet to outlet pressure ratio. Note that, for a given inlet and outlet pressure condition, the rarefaction acts to increase the observed

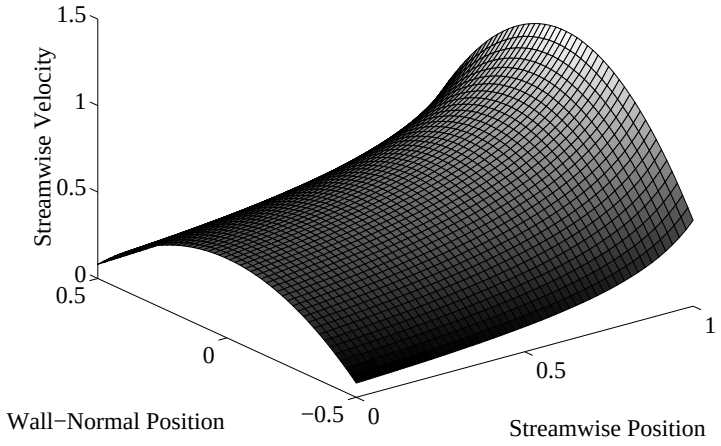

Figure 2.3: Plot of non-dimensional streamwise velocity distribution $\tilde{u}_o(\tilde{x}, \tilde{y})$ in a long microchannel from equation (2.17). The outlet Knudsen number is 0.155 and the pressure ratio is 3, σ_m is assumed equal to unity

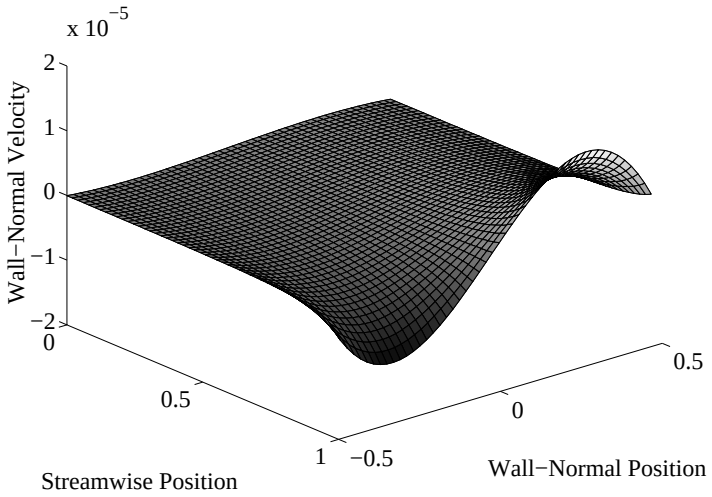

Figure 2.4: Plot of non-dimensional wall-normal velocity distribution $\epsilon\tilde{v}_1(\tilde{x}, \tilde{y})$ in a long microchannel from equation (2.18). The outlet Knudsen number is 0.155 and the pressure ratio is 3, σ_m is assumed equal to unity

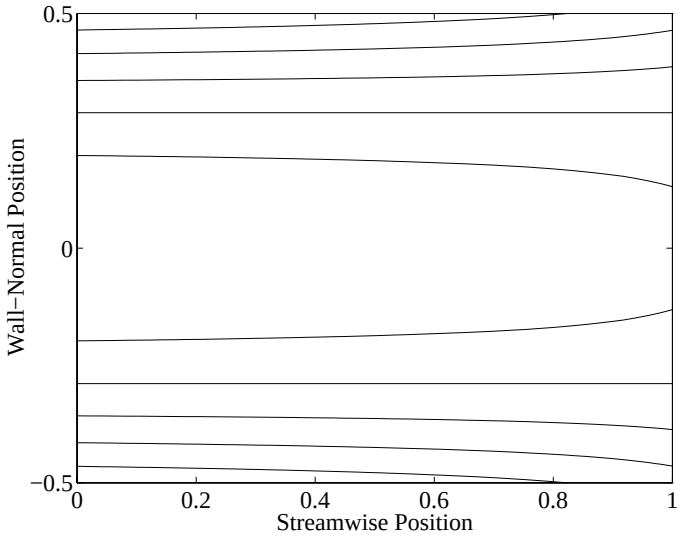

Figure 2.5: Contours of non-dimensional mass flow distribution in a long microchannel. The outlet Knudsen number is 0.155 and the pressure ratio is 3, σ_m is assumed equal to unity

mass flow and that as the pressure ratio decreases, the effect of slip becomes a more significant contribution to the total mass flow. Also, as the outlet pressure increases for a given inlet pressure or as the characteristic dimension increases, the rarefaction contribution diminishes.

With the exception of the TMAC, all variables in this expression are known or are easily measurable. While equation (2.21) is the fundamental expression for channel flow which relates the impact of the slip velocity and, by extension, the value of the TMAC to momentum exchange, extracting values of the TMAC using this expression is exceedingly difficult due to the non-linear functional relationship. However, there exists at least two, more appropriate, ways to represent the data for the purposes of TMAC measurement and they are described below.

2.2.2 Mass Flow Conductance

A valuable expression which can be used to interpret the subsequent experimental results is the mass flow conductance. Making an analogy to Ohm's law where the potential is analogous to the differential pressure applied across the channel (ΔP) and the mass flow is analogous to current, the flow conductance can be defined by:

$$\frac{\dot{m}}{\Delta P} = \frac{H^3 w}{12\mu LRT}\bar{P} + \frac{H^3 w}{2\mu LRT}\frac{2-\sigma_m}{\sigma_m}K_o P_o, \tag{2.22}$$

or

$$\mathcal{C} = \mathcal{A}\bar{P} + \mathcal{B}, \tag{2.23}$$

where $\Delta P = P_i - P_o$ is the differential pressure across the channel, $\bar{P} = (P_i + P_o)/2$ is the mean *measured* pressure (from here on referred to as the mean pressure)[1], $\mathcal{A}$ is a constant given by the channel and gas characteristics and is independent of the TMAC. $\mathcal{B}$ is given by the channel, gas and flow characteristics, including the TMAC.

The flow conductance given in equation (2.22) is linear in mean pressure. If the measured flow conductance is plotted versus mean pressure and is linear as well, then the slope of the experimental conductance can

[1] The mean measured pressure is not the same as the mean pressure within the channel. Because of the non-linear aspect of the pressure drop, the mean pressure defined above is less than the mean pressure within the channel defined by $\frac{\int P dx}{L}$ (see figure 2.2).

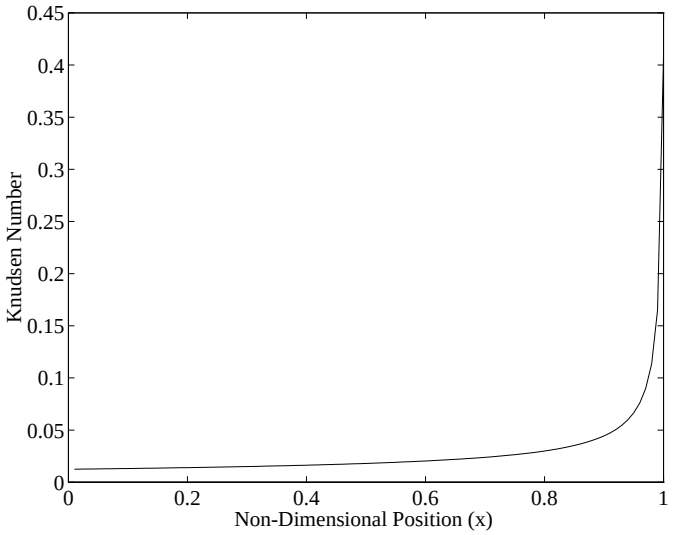

Figure 2.6: Theoretical Knudsen number distribution down the length of a channel for a pressure ratio of 33 and an outlet Knudsen number $K_o = 0.41$.

be used in several ways. Foremost among the ways is as validity check of the slip-flow Navier-Stokes model. Since all variables which appear in the first-order term are well-characterized and independent of the TMAC, if the slope of the measured conductance compares favorably with the slope of the calculated conductance then the slip-flow model is validated. The significance of such a validation is related to two aspects of this study:

1. in order to derive meaningful values for the TMAC, the validity of the slip-flow solution must be established and,

2. there may not be a well-defined Knudsen number to use for slip-flow validation or regime characterization.

Item 1 is discussed in the next section. We discuss item 2 below.

In section 1.1 it was suggested that the magnitude of the Knudsen number could be used for regime characterization and the empirical evidence (Knudsen's original study) as well as the evidence derived from our understanding of the Boltzmann equation was discussed. It was stated that, as long as the Knudsen number remained below a certain value (0.1), the approximations associated with the Navier-Stokes equations were reasonable. However, the specific definition of the Knudsen number to be used for flow characterization was not given. In the case of the channel, it is natural to assume that, because the outlet Knudsen number represents the quantitative contribution of the effects of rarefaction, it can also be used for qualitative regime characterization. However, because of the relatively large pressure ratios encountered in this thesis, we believe that the outlet Knudsen number may overestimate the significance of rarefaction and may not be used for accurate regime characterization. The outlet Knudsen number can be substantially larger than the Knudsen number along the majority of the channel length.

This concept can easily be visualized by assuming that equation (2.20), derived from the slip-flow analysis, accurately represents the pressure distribution within the channel and plotting the theoretical Knudsen number along the length of a channel. For an example of the Knudsen number distribution derived from (2.20) for a single set of flow conditions encountered in this thesis (outlet Knudsen number 0.41 and pressure ratio 33) see figure 2.6. The TMAC is assumed equal to unity for this case.[2]

[2] It will be shown later that a TMAC value near unity may not be the most appropriate value for analysis, but it is used here for purposes of consistency.

Figure 2.6 clearly shows that, for the majority of the channel length (97% in this case) the *local* Knudsen number remains within the slip-flow regime as defined in section 1.1. Therefore we believe that outlet Knudsen number is not the most appropriate Knudsen number to use for regime characterization. Perhaps the Knudsen number based on the mean pressure within the channel or the average of the inlet and outlet Knudsen number would be more appropriate for regime characterization. In any case, if the well-defined outlet Knudsen number can not be used for regime characterization, then other means for slip-flow validation must be employed. In this thesis, the functional relationship of the flow conductance is used for this purpose and the significance of this validity check will be further highlighted when we discuss the experimental results in chapter 5.

In addition to the breakdown of the slip-flow solution due to rarefaction, there are other potential causes for discrepancies between the empirical and theoretical flow conductances. For instance, if the gas is contaminated, then its properties are no longer represented by pure gas properties and this could cause deviation between the model and theory. Or, if the channel deflects appreciably under the pressure from within, then the two-dimensional model used for analysis ceases to be valid, thus causing deviations. While the gas purity may be difficult to check, the amount of channel deflection from the pressure within can be easily estimated. Using a simplified plate model, it can be shown that for all flow measurements made for this thesis the maximum channel deflection remains below 8×10^{-14} m (see appendix C for details). This deflection is considered negligible.

Another use of the measured flow conductance is as a means of determining the TMAC. That is, if the measured flow conductance is linear, the intercept (as $\bar{P} \to 0$) of the measured flow conductance ($\mathcal{B}$) can be used to derive a value for the TMAC. However there is another, more advantageous, way of expressing the data from which the TMAC can be calculated without having to extrapolate the flow results.

2.2.3 Normalization for TMAC Extraction

To extract the TMAC from the flow measurements without having to extrapolate the flow conductance, the mass flow can be normalized or weighted by the difference in the square of the inlet and outlet pressure ($P_i^2 - P_o^2$):

$$\frac{\dot{m}}{P_i^2 - P_o^2} = \frac{H^3 w}{24\mu LRT} + \frac{H^3 w}{4\mu LRT}\frac{2-\sigma_m}{\sigma_m} K_o P_o \frac{1}{\bar{P}}, \tag{2.24}$$

or

$$\frac{\dot{m}}{P_i^2 - P_o^2} = \frac{\mathcal{A}}{2} + \frac{\mathcal{B}}{2}\frac{1}{\bar{P}}, \tag{2.25}$$

where $\mathcal{A}$ and $\mathcal{B}$ are as given above. If the measured mass flow weighted by the inverse of the difference between the squares of the inlet and outlet pressures, $\frac{\dot{m}}{P_i^2 - P_o^2}$, is plotted versus inverse mean pressure $\frac{2}{P_i + P_o}$ and is linear, then the slope of this plot can be used to extract the TMAC. This method of TMAC extraction is similar to the Temperature Jump (TJ) method which is used to derive experimental values for the energy accommodation coefficient [18].

Although the expression $\frac{\dot{m}}{P_i^2 - P_o^2}$ lacks the appealing physical interpretation of flow conductance, it has the benefit of accentuating variation in the TMAC. That is, instead of having to use the definition of flow conductance and *extrapolate* to find the TMAC, the TMAC is embedded in the first-order term ($\frac{\mathcal{B}}{2}$) of this linear (in $1/\bar{P}$) equation. It is this weighting that is subsequently used in this thesis to derive values of the TMAC.

Chapter 3

Microchannel Fabrication

The TMAC has been shown to be a function of the surface as well as of the gas and, in order to make meaningful measurements of the TMAC, it is critical that the top and bottom of the channels possess as near an identical surface structure as possible. Previous studies of gas flow in micromachined channels, including the work of Pong *et al.* [30] (Caltech/UCLA collaboration) and Harley *et al.* [16] (UPenn) did not possess identical surface structure throughout the channel. In the case of Harley *et al.*, the channels were etched in silicon, using a timed process and the channel was sealed by bonding a top layer of glass to the silicon. The peak-to-valley surface roughness for the etched silicon substrate was reported to be 5 nm [36]; there were no data reported on the surface roughness of the glass cover. For the case of Pong *et al.* the channels were fabricated using phosphosilicate-glass (PSG) as a sacrificial layer with the bottom of the channel being silicon and the top of the channel being silicon nitride. No information on the surface roughness of either the top or the bottom of the channel were reported. Schematic representations of the channel cross-sections for these studies are shown in figure 3.1.

In order to provide near-identical surface structure, we employed a two wafer fabrication process. The process consists of a channel wafer and a capping wafer. With the technique, described below, we fabricated two types of channels each with nominal heights of 1.33 μm.

To begin microchannel fabrication, the channel wafer is back-side polished. Subsequent fabrication is illustrated in figure 3.2 and the detailed process is given in appendix F. The main feature of this procedure is that the channel is not etched in the silicon of the channel wafer. Instead, an oxide is grown on the channel wafer and the channel is etched in the oxide. The oxide thickness defines the channel height and is uniform across the wafer. Once the oxide is grown, it is then patterned and etched in buffered HF. After etching the channel, silicon nitride, which is used as a mask for subsequent KOH etching, is deposited on the wafer. The nitride on the back side is then patterned and etched. The back side ports are etched in a 20% KOH : H_2O solution at 56.5 °C for 29 hours until the etch stops on the front side silicon nitride. The final step in processing the channel wafer is the removal of the silicon nitride in a hot phosphoric etch.

The capping wafer is a n-type <100> prime wafer of any resistivity. It is used to seal the channel wafer.

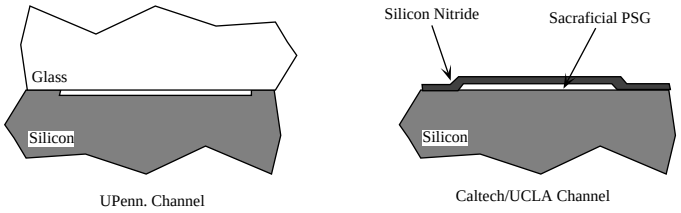

Figure 3.1: Schematic representation of the cross section of other published micromachined channel experiments. The left-hand side represents the channel from the UPenn group and the right-hand side represents the channel of the Caltech/UCLA collaboration.

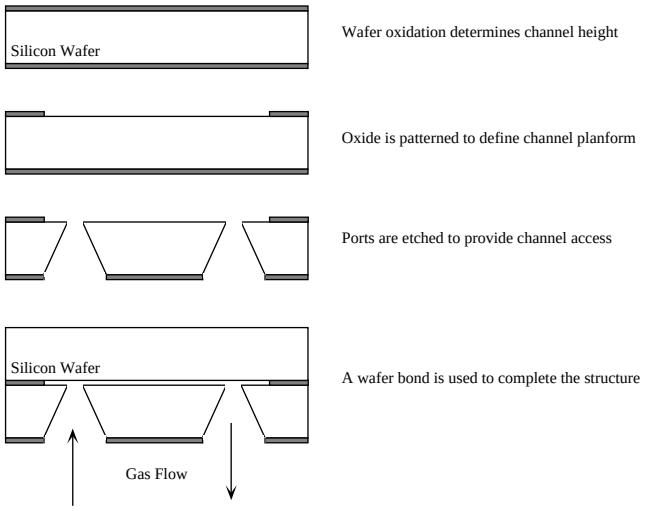

Figure 3.2: Schematic representation of the primary fabrication steps.

To seal the channels by bonding the capping wafer to the channel wafer, the two wafers undergo a standard pre-oxidation wafer clean and are then contacted in a clean room. After contact, the wafers are inspected for contact voids with an infrared inspection system. The bonding is completed with an anneal in nitrogen at 1000 °C for 70 minutes[37]. This anneal completes the bond and seals the bonded interface. The wafers are then re-checked under the infrared source for post-anneal voids. The yield for this process is approximately 95%.

Prior to the bonding procedure, the geometric characteristics of the channel are determined. The length of the channel is measured optically and is 7490 μm $\pm 1 \mu$m. The width of the channel is taken as the mean of the top and bottom of the channel (see figure 3.6). This measurement is made at ten positions along the length of the channel using a calibrated scanning electron microscope and the mean value of these measurements is 52.3 μm. Two standard deviations around the mean (0.3 μm) are taken as the uncertainty in the channel width. The depth is measured using a mechanical stylus profilometer at five positions along the length of the channel. The profilometer measurements are further verified with interferometric measurements of the oxide thickness. The channel height is taken as the mean of the five interferometric measurements (1.33 μm) and the uncertainty in the channel height is taken as two standard deviations around the mean (0.01 μm). The surface roughness for the channel wafer and capping wafer was measured using a Wyko Corporation non-contact surface profilometer and the typical r.m.s. surface roughness was found to be less than or equal to 0.65 nm [38]. Representative data are shown in figure 3.3.

The fabrication sequence described above was carried out twice with two separate mask sets. The mask geometries are shown in appendix E. One hundred thirty-five channels were fabricated; three were tested. The fabrication results are given in Tables 3.1 & 3.2. Scaled schematic drawings of each of the respective channel types are shown in figures 3.4 and 3.5. The primary difference between Channel 1 and Channel 2 is the width of the channel. Another difference between Channel 1 and Channel 2 is the configuration of the entrance and exit of the channel. For Channel 2, entrance and exit of the channel coincides with the front-side access port (the black squares in figure 3.5). In the case of the Channel 1 type, there is a twenty micron "entrance region" between the access ports and the channel opening. The specific flow histories of the channels tested are given in appendix B.

A scanning electron micrograph of the Channel 1 cross section is shown in figure 3.6. Because an isotropic etch is used to etch the oxide, the width of the channel is not constant throughout the depth of the channel

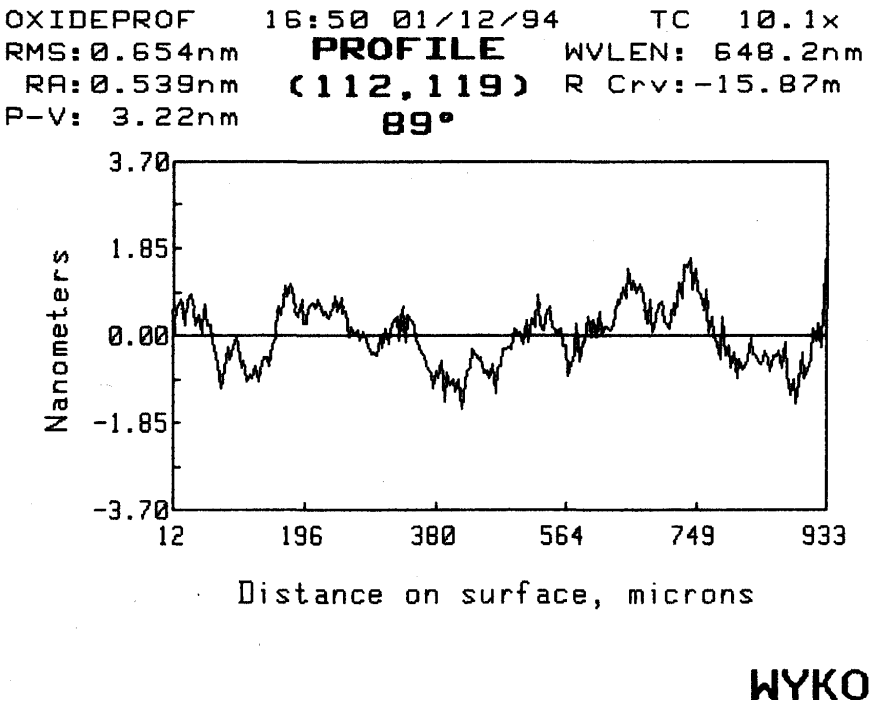

Figure 3.3: Representative surface roughness data.

Parameter	Nominal Value(μm)	Uncertainty(μm)
length (L)	7490	± 1
width (w)	52.3	± 0.3
height (H)	1.33	± 0.01
surface roughness	$\leq 0.65 \times 10^{-}3$	NA

Table 3.1: Results of microchannel characterization for Channel 1, wafer bond completed 4/10/94.

(see figure 3.6). To compensate for this variable width of the channel, we define the width w as the mean of the actual channel width at the top and bottom of the oxide. Because the aspect ratio of the channel is so large (approximately 39 for Channel 1 and 77 for Channel 2), the effect of the variation of the width of the channel on the dynamics of the flow caused by the isotropy of the oxide etch is negligible.

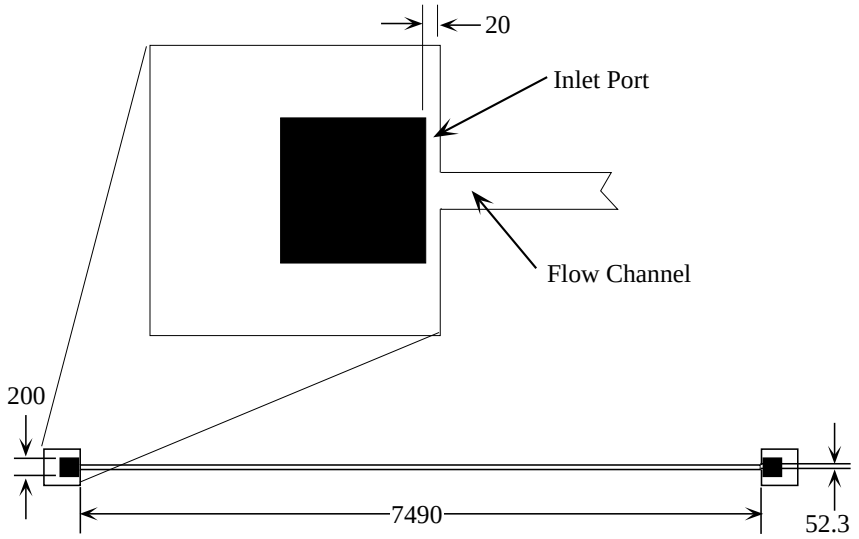

Figure 3.4: Schematic representation of Channel 1.

Parameter	**Nominal Value(μm)**	**Variation(μm)**
length (L)	7530	± 1
width (w)	102.3	± 0.3
height (H)	1.33	± 0.01
surface roughness	$\leq 0.65 \times 10^{-}3$	NA

Table 3.2: Results of microchannel characterization for Channel 2, wafer bond completed 6/12/96.

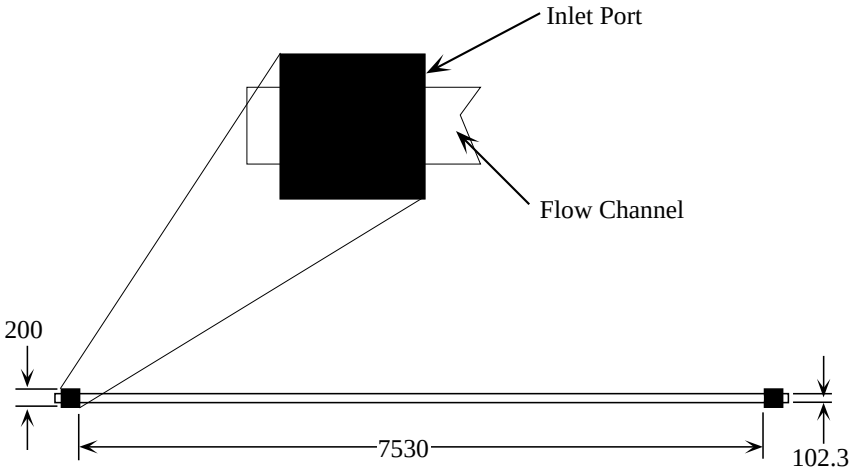

Figure 3.5: Schematic representation of Channel 2.

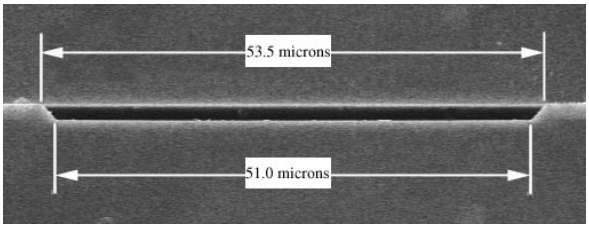

Figure 3.6: Scanning electron micrograph of Channel 1 cross section.

Chapter 4

Mass Flow Hardware

To extract meaningful values of the TMAC, the mass flow due to slip must be resolved and, from equation (2.21), this is given by:

$$\dot{m}_{\text{slipflow}} = \frac{H^3 w}{2\mu LRT}\left(\frac{2-\sigma_m}{\sigma_m}K_o P_o(P_i - P_o)\right). \tag{4.1}$$

For characteristic pressures ($P_o = 101$ kPa, $P_i = 124$ kPa) assuming complete accommodation, the mass flow through the channel for argon flowing in Channel 1 due to the presence of slip is approximately 7×10^{-13} kg/s or 2×10^{-11} mol/s (approximately 20% of the total mass flow).

4.1 Low-Flow Measurement

Although low-flow or leak measurements are used extensively in non-destructive testing of pressure vessels, as of 1994, no commercial equipment was available for calibrating flow rates below 10^{-6} mol/s [39]. We are now aware of secondary-sensors commercialized by the Yokogawa Corporation of America which are capillary-based and have the ability to measure down to approximately 10^{-9} mol/s [40]. The flow rates which must be resolved for this study are of the order 10^{-11} mol/s, at least five orders of magnitude below that which commercially-available sensors (as of 1994) would resolve and still two orders of magnitude below the current state of the art. The compelling need to measure flow rates below that which commercially available sensors could measure was the impetus to develop the mass flow system outlined in this chapter.

4.1.1 Primary Flow Meters

Gas flow rate is defined as the number of moles passing through a system during a given time interval. Due to current technical limitations, primary flow meters can not directly measure this flux but must infer it based on an equation of state. The appropriate equation of state for the conditions which we are interested in that is sufficient for the required level of accuracy[1] is the ideal-gas equation of state (2.4). In molar terms may be written as:

$$pV = NRT, \tag{4.2}$$

where V is the volume of the system, N is the number of moles and R is the gas constant. A primary measurement can then made and the molar flow rate is given by:

$$\frac{dN}{dt} = \frac{d}{dt}\left(\frac{pV}{RT}\right). \tag{4.3}$$

[1] The maximum deviation from the ideal gas law for the test conditions of this thesis is discussed in appendix A and is shown to be ≤ 2 %

If the mass flow as opposed to the molar flow is desired, then the *specific* gas constant ($\mathcal{R}$) can be used and the *mass flow* is given by:

$$\frac{dm}{dt} = \frac{d}{dt}\left(\frac{pV}{\mathcal{R}\mathcal{T}}\right). \tag{4.4}$$

For practical purposes, when a primary flow meter is developed based on an equation of state, either the pressure or the volume of the flowmeter is allowed to vary in time and thermal fluctuations are minimized by thermal isolation. These techniques are known respectively as constant-volume and constant-pressure techniques. Together, they represent the fundamental means by which primary flow measurements are made [41].

The constant-pressure technique is described by McCulloh *et al.* [41] and is based on regulating the flow by decreasing or increasing the volume of the system while maintaining constant pressure within the system. The approach is straightforward and elegant yet, for small flows near standard pressure, the necessity to measure minute volume changes can be prohibitive. For instance, at atmospheric pressure and room temperature assuming there is no temperature fluctuation of the system ($dT/dt = 0$), to measure flow rates of the order 10^{-10} mol/s, the required rate of change in volume of the system must be of the order $10^{-11}\text{m}^3/\text{s}$. If one is using a piston to change the volume of the system, and the piston has a cross-sectional area of 1 cm^2, the rate of advancement of the piston must be of the order 10^{-7} m/s. Of course a much smaller piston can be used, but for the technique to be accurate, the piston area must be well characterized. This approach also requires high-integrity seals on the piston or, as has been suggested, a welded bellows to decrease the volume of the system [41].

4.1.2 Single-Tank, Constant-Volume System

For a constant-volume technique, assuming a quasi-steady process, the mass flow for an ideal gas into a system is given by:

$$\dot{m} = \frac{V_s}{\mathcal{R}T_s}\frac{dp_s}{dt} - \frac{p_s V_s}{\mathcal{R}T_s^2}\frac{dT_s}{dt}, \tag{4.5}$$

the subscript s refers to system properties. In this approach, as long as the volume of the system is known and the process is quasi-steady, the flow rate is determined by measuring the pressure and temperature of the gas as a function of time. While this technique is inherently less complicated than the constant-pressure technique, a direct application of this technique, commonly referred to as an accumulation technique, is insufficient for our purposes. For instance, at atmospheric pressures and for the flow rates of interest, the change in pressure for a 100 cc tank is approximately on the order of a few Pascal over several minutes. To resolve these pressure changes would require an absolute pressure sensor that has a dynamic range of six orders of magnitude. In addition, this approach possesses severe thermal stability requirements[2]; a system with the required flow resolution and a volume of 100 cc operating at atmospheric pressure requires a drift in temperature of less than 10^{-6} K/s.

It is interesting to note that, if one is measuring comparable flow rates at pressures significantly less than atmospheric, the requirements on the drift in temperature are greatly reduced. As an example, if the system pressure is approximately 1 Pa ($8 \times 10^{-}3$ torr), then the required temperature stability is reduced by five orders of magnitude. The National Institute of Standards and Technology has developed a *constant-pressure* system which operates at reduced pressure that has been shown to be able to resolve flow rates on the order of 10^{-11} mol/s [41]. More recently, others have established an ability to make similarly resolved measurements [42].

Of course, to decrease the thermal sensitivity, the system volume could be reduced but the size of the system volume is limited by the the dead volume associated with high-resolution pressure sensors. Another way to theoretically reduce the thermal sensitivity, is to substantially increase the temperature of the system. However, even if the temperature could be doubled, the thermal requirements would only be reduced by a factor of four.

[2] The constant-pressure approach discussed above also has similar thermal restrictions.

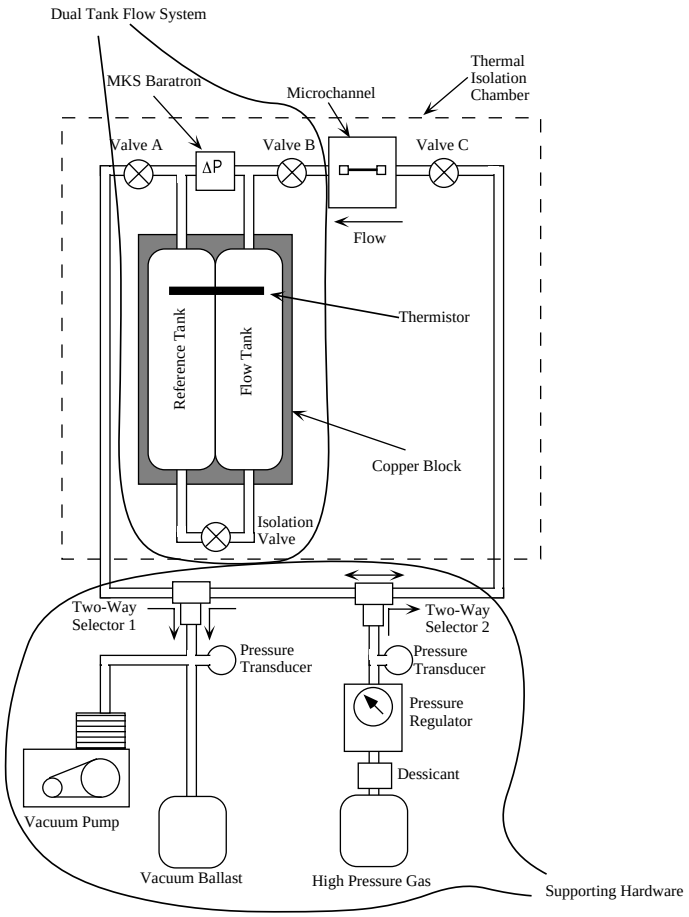

Figure 4.1: Schematic representation of the test platform (data acquisition system not shown).

4.1.3 Dual-Tank, Constant-Volume System

It has been shown above that the required temperature stability for the constant-volume primary flow standard at the pressures and flow rates of interest prohibits the direct application of this approach. It is currently difficult to assure that the gas temperature within the system is steady to within 10^{-6} K/s. To mitigate the extreme thermal sensitivities associated with the constant-volume accumulation approach, we have developed a two-tank modified constant-volume accumulation technique. A schematic representation of the two-tank system is shown in figure 4.1.

In the two-tank approach, instead of measuring the change in absolute pressure as a given tank is charged, the change in differential pressure between two tanks is measured as one tank (flow tank) is filled and the other tank (reference tank) remains in steady state. The flow for such a system is given by:

$$\frac{V_f}{\mathcal{R}T_f}\frac{dp_f}{dt} - \frac{V_r}{\mathcal{R}T_r}\frac{dp_r}{dt} = \dot{m}_f + \frac{p_f V_f}{\mathcal{R}T_f^2}\frac{dT_f}{dt} - \frac{p_r V_r}{\mathcal{R}T_r^2}\frac{dT_r}{dt}, \tag{4.6}$$

where the subscript r refers to the gas within the *reference* tank and the subscript f refers to the gas within the *flow* tank.

If the two tanks are at the same temperature,

$$T_r = T_f \tag{4.7}$$

and the tanks undergo identical thermal fluctuations,

$$\frac{dT_r}{dt} = \frac{dT_f}{dt}, \tag{4.8}$$

then the flow for this two-tank system is given by:

$$\dot{m} = \frac{V_f}{\mathcal{R}T_f}\frac{d\Delta p}{dt} - \frac{\Delta p V_f}{\mathcal{R}T_f^2}\frac{dT_f}{dt}, \tag{4.9}$$

where $\Delta p = p_f - p_r$. The sensitivity to thermal fluctuations $\frac{dT_f}{dt}$ of the two-tank approach is reduced by five orders of magnitude over that of the one-tank accumulation approach i.e., Δp is approximately five orders of magnitude smaller than p.

The stipulation of equal temperatures $T_f = T_r$, and equal thermal responses $\frac{dT_f}{dt} = \frac{dT_r}{dt}$ in the above analysis implies that the tanks must possess sufficient thermal coupling so that, over the time scale of the experiment, the tanks possess identical thermal histories. If the tanks possess identical thermal histories, this two-tank approach will exhibit common-mode thermal rejection and the severe thermal sensitivities associated with the single-tank approach will be reduced. Two phenomena which may invalidate the above stipulations are ambient-induced thermal fluctuations and thermodynamically-induced changes associated with the fact that the gas within the flow tank has a tendency to change temperature as gas enters the flow tank. If the tank does not represent a constant-temperature heat sink (or source, depending on direction of the change in temperature i.e., the sign of the Joule-Thompson coefficient) to the gas, then the flow into the tank will not be isothermal and the differential pressure between the reference and flow tank will not be exclusively a result of the increase in the amount of gas in the flow tank. Each of these phenomena will be subsequently discussed in section 4.3.1.

4.2 Test Hardware

A schematic representation of the test hardware is shown in figure 4.1. The hardware consists of three separate functional groups: the-dual tank flow system, the microchannel and the supporting hardware. The dual-tank system which is used to make the flow measurement and the supporting hardware which is used to establish the flow are outlined in the figure. A more detailed representation of the dual-tank system is given in appendix D. O-rings are used to interface the channel to a manifold which in turn is welded to the hardware.

All valves of the dual-tank system are pneumatically-actuated, high-integrity Nupro ss4BK bellows-sealed valves. On the isolation valve, the pneumatic actuator is controlled through a Bellofram type 1000 voltage-controlled pressure regulator. The tanks are standard Nupro high-pressure stainless steel tanks with nominal volumes of 50 cc and are enveloped in a machined block of copper with a mass of approximately 5 kg. The piping is quarter-inch stainless steel and the differential pressure transducer is an MKS type 120, 1 torr Baratron with an uncertainty of 1.3×10^{-3} Pa. The Baratron is connected to the system by means of metal gasket face seal fittings. All of the piping and valves are welded in place. The system including all valves, the tanks, the differential pressure transducer and the microchannel is placed inside an insulated housing to reduce the effects of ambient thermal fluctuations. An Omega high-precision ($\pm 0.01^\circ$C) thermistor is used to measure the tank temperature.

The supporting hardware can be broken down into two parts: that which is used to impose and measure the inlet pressure to the channel and that which is used to set the outlet pressure of the channel. The outlet pressure is the nominal pressure within the reference and flow tanks and is set by means of a standard roughing pump. This pressure is measured with a Honeywell type 242 $\pm$15 psig pressure sensor with an uncertainty of 140 Pa and for our experiments the pressure ranges from approximately 13 kPa to 101 kPa. The inlet pressure is controlled by means of a Bellofram type 1000 voltage-controlled pressure regulator and is corroborated with the use of a Honeywell type 242 0-100 psig pressure sensor. The uncertainty of this Honeywell transducer is 690 Pa. For our experiments, the inlet pressure ranges from approximately 130 kPa to 427 kPa. Atmospheric pressure is measured with a Honeywell type 140 $\pm$15 psia pressure sensor with an uncertainty of 140 Pa. All the pressures measured with the Honeywell sensors are verified with a high-accuracy Setra type 370 100 psia sensor which has an uncertainty of 7 Pa.

4.3 Test Procedure

To measure the flow of gas through the channel, we measure the time-dependent differential pressure between the flow and reference tank as well as the temperature of the two tanks and use equation (4.9) to reduce the data.

Before each test, the reference tank and flow tank are set to the test outlet pressure to be imposed on the channel. This is accomplished by opening valves A, B, C and the isolation valve and setting the pressure by adjusting the pressure with the vacuum pump. The pressure is recorded, valve A is closed and the system is allowed to settle. The isolation valve is then closed. Because all valves are pneumatically-controlled bellows valves, upon closing, they inject gas mass into the piping due to the compression of the bellows. It has been found that this mass injection due to the closing of the isolation valve tends to set up thermal transients and that the closing of the isolation valve should be done in a gradual manner. The pneumatic-actuation and voltage-control of the isolation valve allow the isolation valve to be closed by slowly increasing the pressure to the valve actuator. The procedure used to close the isolation valve includes a slow ramp of the closing pressure with feedback of the differential pressure from the Baratron used to control the closing rate. In a standard run, it takes approximately 30 minutes to close the isolation valve completely.

After the isolation valve is closed and before the test is begun, the system is allowed to settle for 10 minutes. Each flow test consists of three 10 minute intervals when the differential pressure across the tanks is measured: pre-flow measurement, flow measurement and post-flow measurement. To begin the test, the differential pressure is recorded for 10 minutes before the microchannel is pressurized. Then flow is initiated through the channel by increasing the inlet pressure of the microchannel to the desired value, this is done by means of the voltage controlled pressure regulator. It has been found that by ramping the pressure, we minimize thermal effects on the piping and that a ramping time of 10 seconds is sufficient for our purposes. After the pressure is ramped to the desired test value, the differential pressure is recorded for an additional 10 minutes. This differential pressure signal is the change in pressure associated with the flow of gas. To stop the flow, the pressure is ramped back down over a time period of 10 seconds. After the flow through the resistance is stopped, the differential pressure is recorded for another ten minutes. All signals are acquired at a rate of 1 sample per ten seconds with a twelve-bit National Instruments A/D, D/A card interfaced to a Gateway 486 computer.

We use this three-segment approach to measure the ambient-induced thermal fluctuations as well as to check for thermodynamically-induced fluctuations. Ambient-induced fluctuations appear as a continuous smooth variation in the differential pressure signal throughout the entire test and can be filtered. However, thermodynamically-induced changes or non-isothermal conditions within the flow tank appear in the post-flow measurement of the differential pressure alone and currently can not be filtered. Because they can not be filtered, the thermodynamically-induced changes determine the upper limit on the flow rate beyond which which this technique can not be used to accurately measure flow.

Thermodynamically-induced changes are a function of the flow rate and appear when the flow across the channel is sufficiently large such that the tank can not be considered a constant-temperature heat sink. For the channels used in our tests, this variation is discernible at inlet pressures above 441 kPa and never discernible at pressures below 427 kPa. Although we believe that the *flow rate* is the cause of thermodynamically-induced variation and sets the upper limit on the flow which this setup can accurately measure, because pressure is the control variable, it is useful to know at what *pressure* this upper limit is reached.

4.3.1 Flow Experiments and Data Reduction

As stated above, we use a three-segment approach for flow experiments to measure the ambient-induced thermal variations. This is done in order to filter the ambient-induced thermal signals which, if present, will cause a change in differential pressure which is indistinguishable from the flow-induced signal. To filter the ambient-induced signal, it is assumed that the differential pressure throughout the experiment is a linear combination of two phenomena: ambient-induced variations and flow-induced changes in differential pressure (see figure 4.2). Furthermore, it is assumed that flow-induced changes are only present when the microchannel is pressurized. On the basis of these assumptions, the thermally-induced variations can be filtered by undertaking a piecewise non-linear least-squares fit to the data. The thermally-induced signal is

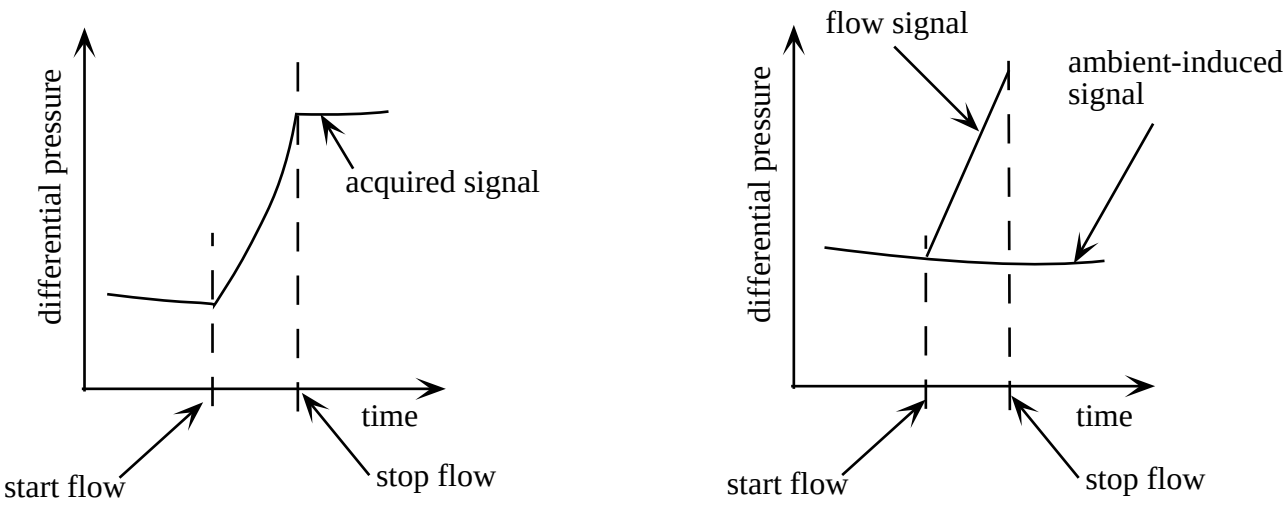

Figure 4.2: Schematic representation of single flow experiment. It is assumed that the differential pressure is a linear combination of two phenomena: ambient-induced thermal signals and flow-induced signals. An ambient-induced thermal signal is present throughout the test and the flow-induced signal is only present for a portion of the experiment (when the channel is pressurized).

fitted with a least-squares second-order polynomial from 0 to 1800 seconds. The flow-induced signal is fitted with a linear least-squares from 600 to 1200 seconds. The slope of the linear least-squares plot is then taken as the change in differential pressure due to the flow, $\frac{d\Delta P}{dt}$ and is used in equation (4.9) to determine the flow rate.

Examples of results from two argon flow experiments are given in figure 4.3. The tank pressures are set to atmospheric pressure (101 kPa) and the microchannel is pressurized to a value of 146 kPa. The left hand side of the figure is from a test in which thermally-induced signals are negligible. As proven by the fact that the pre-flow and post-flow differential pressure signals are constant, there is no change in pressure between the two tanks due to thermal fluctuations. In this case, regardless of whether or not the least-squares filtering is used to reduce the data, the flow rate is determined to be 12.2×10^{-12} kg/s. The data on the right hand side of figure 4.3 are representative of a test when the thermally-induced signals are non-negligible. In this case, the thermally-induced signal must be filtered using the least-squares approach described above. Typically, the thermal signals are negligible, and the vast majority of experiments resemble the left hand side of the data shown in figure 4.3. However, to be consistent, the least-squares method described above is always used for the purposes of making flow measurements.

Another interpretation of the pre-flow and post-flow non-constant differential pressure signals shown on the right-hand side of figure 4.3 is that a leak is present in the system causing this change in differential pressure. However, we are confident that the phenomenon is not leak-generated because over multiple runs, when the pre- and post-flow changes in differential pressure are present, the pre- and post-flow signal variably occurs in both the positive and negative directions. A leak, if present, would cause a systematic change in differential pressure that would be consistently positive or negative depending upon which side of the isolation valve was leaking.

Although we can account for ambient-induced variations with the piecewise curve fit, the results of which are shown in the right-hand side figure 4.3, thermodynamically-induced variations can not be easily filtered and we believe that these variations result in an upper limit beyond which this system can not be used to accurately measure the flow. Data for a case where we believe thermodynamically-induced fluctuations are present are shown in figure 4.4. Note the significant variation in the functional relationship of the pre-flow and post-flow differential pressure signal. We interpret this variation as caused by a non-isothermal flow of the gas into the flow tank. It has been found that, as long as the pressure at the inlet is kept below 427 kPa, this type of post-flow signal does not occur. For pressures at or above 441 kPa, this type of signal, which

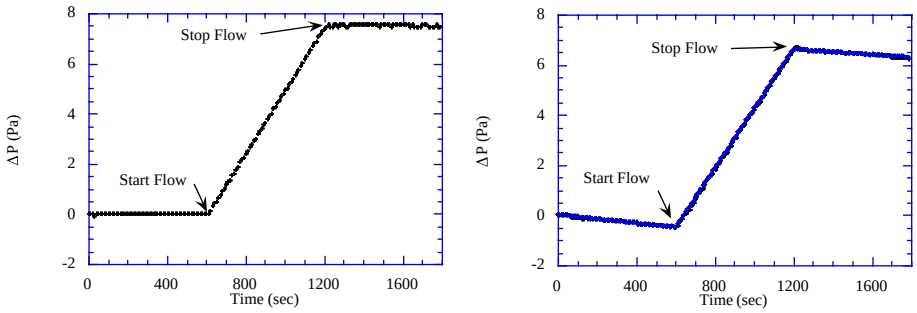

Figure 4.3: Representative flow experiments of argon, with the inlet to the channel set at 146 kPa and the outlet pressure set to 101 kPa. On the left-hand side, it can be seen that thermal fluctuations are negligible compared to the flow signal. On the right-hand side, the thermal fluctuations are non-negligible. In both cases, the flow rate is given by the slope of the first-order curve fit from 600 to 1200 seconds and equation (4.9). It is 12.2×10^{-12} kg/s.

always possesses negative-curvature, appears. As mentioned above, we believe that it is the flow rate and not the pressure imposed across the channel that causes this type of post-flow variation in the differential signal and we also believe that this post-flow differential pressure fluctuation is likely a function of the flow and reference tank pressure as well as the gas, though this has not been tested.

As a final comment on the post-flow pressure fluctuation it is interesting to note that a similar, though significantly larger in both magnitude and extent, signal occurs if the isolation valve is not closed slowly. We interpret this similarity in pressure fluctuations as further evidence that this type of post-flow signal is dependent on the change in pressure within the flow tank (gas injected into the tank).

4.3.2 Mass Flow Resolution

In an attempt to assess the resolution of this approach, the microchannel was replaced with solid piece of pyrex and identical experiments as those described above were undertaken. The tanks were set to a pressure of 15 kPa and the flow resistance (solid pyrex) was pressurized to a value of 427 kPa. Under these conditions and using the least-squares data reduction method described above, we measured a flow rate of 7×10^{-15} kg/s. This can be compared with the theoretical limit on the resolution due the Brownian motion of the gas within the system and to the resolution due to the pre-amplifier noise of the MKS Baratron.

Because the mass flow system described above measures the mass flow (change of the mass of the gas within the flow tank per unit time) based upon the change in differential pressure between the flow and reference tanks, the resolution of this approach is fundamentally limited by the differential pressure fluctuations associated with Brownian motion of the gas which is in contact with the surfaces of the sensor. It can be shown that the signal-to-noise ratio (where the noise is generated from Brownian motion) for this system is given by [43]:

$$SNR = \frac{(\Delta p A)^2}{4\kappa T D}, \tag{4.10}$$

where Δp is the differential pressure imposed on the sensor (related to mass flow), A is the sensor area, κ is the the Boltzmann constant, T is the temperature of the gas and D represents the squeeze film damping of the sensor. Because the gap between the sensor diaphragm and the sensing electrodes in the Baratron is $\approx$ 75 μm [44], a continuum hypothesis with no-slip at the wall is well-justified and the damping term can be shown to be: [43]

$$D = \frac{3\mu A^2}{2\pi {h_o}^3}, \tag{4.11}$$

where μ is the gas viscosity and h_o is the initial height of the air gap between the sensor head and the sensing electrodes ($\approx$ 75 μm). With this expression for the damping, the required change in differential pressure for

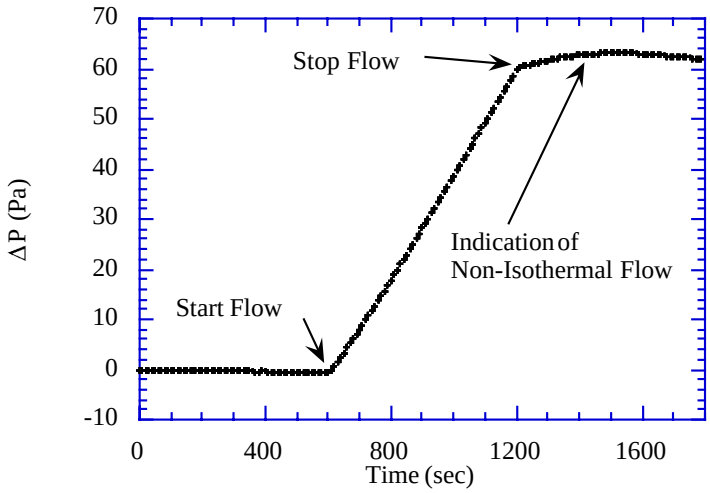

Figure 4.4: A representative argon flow experiment where the flow rate is sufficiently large to cause post-flow fluctuations. We interpret this rise as a thermodynamically-induced fluctuation associated with the heating of the gas within the flow tank and we believe that this phenomenon sets the upper limit for the flow rate which this technique can accurately measure.

a given signal-to-noise ratio can be shown to be:

$$\Delta p = \sqrt{\frac{6SNR\kappa\mu}{\pi h_o^3}} \tag{4.12}$$

In order to obtain a signal to noise ratio of 1000 for argon ($\mu \approx 21 \times 10^{-6}$ Pa s), the change in differential pressure associated with this minimally resolved flow would need to be $1.5{\times}10^{-6}$ Pa. For a ten minute run, this corresponds to a theoretical mass flow resolution of $4{\times}10^{-18}$ kg/s.

The theoretical resolution of the system based on the preamplifier noise of the MKS Baratron can also be calculated. To do so, we use the reported resolution of the MKS Baratron which is 1.3×10^{-3} Pa. If this is measured over a ten minute run, then the the theoretical mass flow resolution is calculated to be $9{\times}10^{-16}$ kg/s. The practical theoretical resolution, based on the pre-amplifier noise of the MKS Baratron is an order of magnitude smaller than the estimate of the resolution obtained with the pyrex experiment. We believe that the resolution of the analog to digital conversion which occurs during the signal acquisition is the most-likely cause for this discrepancy.

4.4 Volume Measurement

In order to use equation (4.9) to reduce the data and obtain the flow rate, an accurate value for the flow volume (V_f) must be known. This volume includes all the relevant contributions of the piping, valves and sensor as well as the flow tank. The approach used in this thesis to accurately and easily measure the entire volume of the flow system in a manner that is independent of flow dynamics is described below. The basic concept consists of replacing the channel with a syringe and using the the syringe to alter the volume of the flow side of the system while monitoring the change in differential pressure within the system. A schematic of the test setup for the system volume calibration is shown in figure 4.5. For the tests described above, as long as there is no leak in the system, and the gas obeys Boyle's law (remains ideal), it is easy to show that the system volume is given by:

$$V_f = \frac{\Delta V_f P_{s,i}}{\Delta P}\left(1 + \frac{\Delta P}{P_{s,i}}\right), \tag{4.13}$$

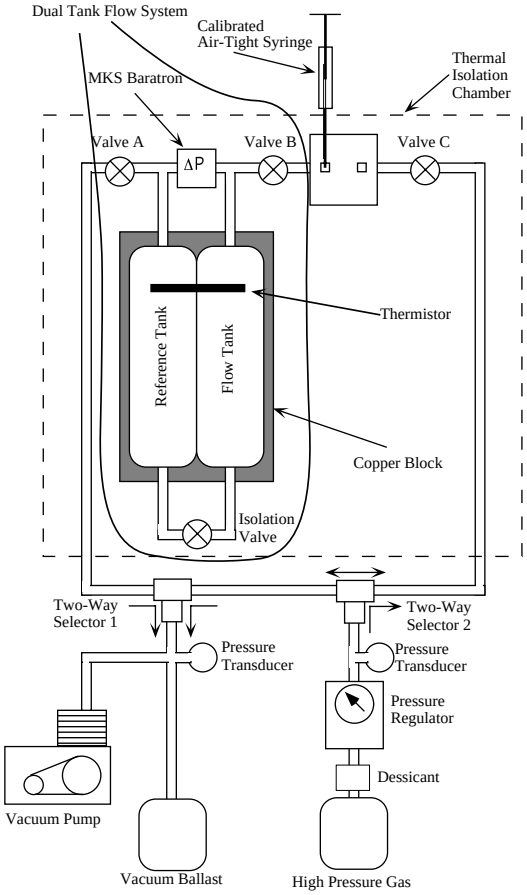

Figure 4.5: The setup which is used to characterize the flow volume. As the syringe is actuated, the differential pressure changes and, using Boyle's law, the flow volume can be calculated

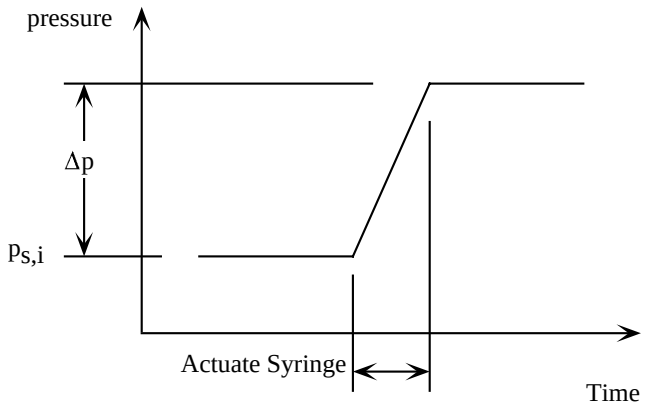

Figure 4.6: Schematic representation of data from volume calibration measurement

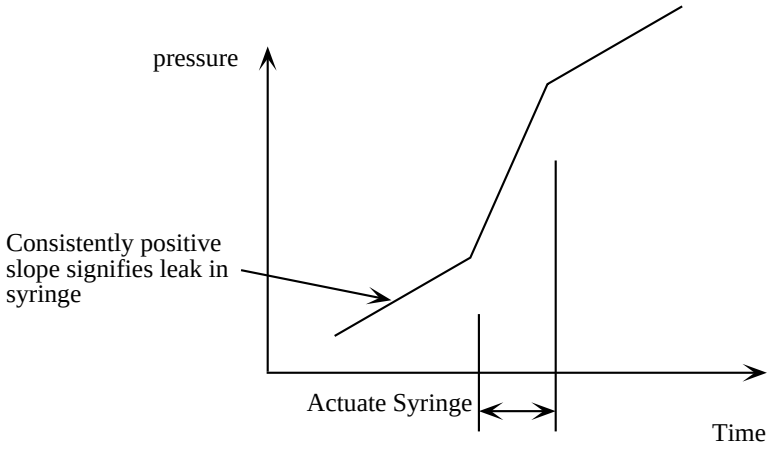

Figure 4.7: Schematic representation of data from a volume calibration measurement in the presence of a leak. The change in the pressure associated with the pre- and post-actuation of the syringe is is believed to be the result of a leak in the syringe and is characteristic of measurements taken below 41 kPa.

where ΔV_f is the volume of the syringe, $P_{s,i}$ is the initial system pressure and ΔP is the change in pressure associated with the syringe actuation. In this experiment, the differential pressure is monitored as the syringe is activated and a schematic representation of the data is shown in figure 4.6.

As mentioned above, as long as no leak is present, this syringe technique can be used to easily and accurately measure the relevant volume of the system but this technique is limited by the seal integrity of the syringe. As the tank pressure is decreased below atmospheric, the sliding seal between the plunger and the internal bore of the syringe will have a differential pressure imposed across it and at a certain pressure will start to leak. Because of the sensitivity of the differential pressure sensor used in this setup, even slight leaks through the syringe are detectable. These leaks appear as changes in the measured differential pressure. However, with a liberal coating of vacuum oil, we have been able to conduct leak-tight (to within the resolution of the differential pressure sensor) volume measurements down to tank pressures of 41 kPa. At pressures below 41 kPa, a leak is present and a schematic representation of data for a volume characterization measurement in the presence of a leak from the syringe is shown in figure 4.7. The presence of a leak within the syringe makes the definition of the terms ΔP and $P_{s,i}$ in equation (4.13) difficult but, as long as the tank pressure remains at or above 41 kPa, no leak through the syringe is detectable.

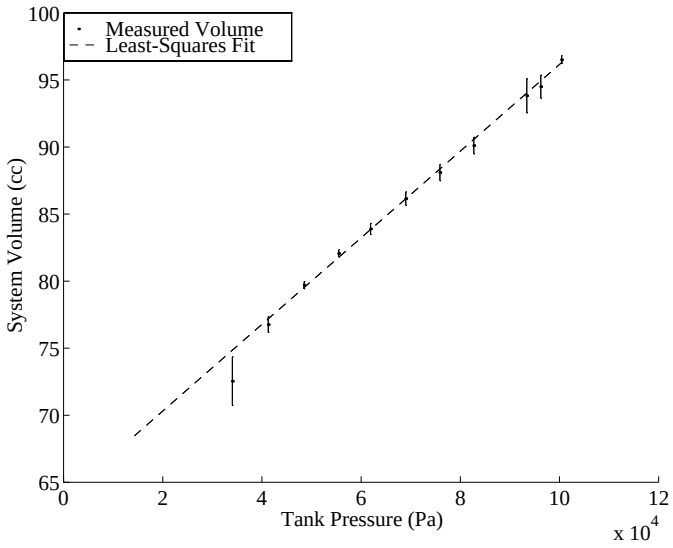

Figure 4.8: Results from the volume-measurement experiment. To determine the least-squares fit, the data point at 34 kPa is neglected. The extrapolation of the least-squares fit is undertaken in order to derive a system volume for all tank pressures used in this thesis.

With a well-defined limitation on this method set by the leak through the syringe, we have undertaken a series of volume measurements at various tank pressures. The results of these tests are shown in figure 4.5. The error bars represent 95% confidence intervals based on a series of 12 measurements.

Figure 4.8 demonstrates that there is a clear and significant pressure dependence of the flow volume. We attribute the pressure dependence of the system volume to the presence of the bellows within the valves (the relevant valves are the isolation valve and valve C) and with the differential pressure sensor (an MKS Baratron). This variation of the system volume with tank pressure was unanticipated in the design of the platform.

Fitting the data presented in figure 4.8 with a linear least-squares model to obtain the pressure-volume dependence of the system, is straightforward and the result used for all subsequent measurements is given by the following expression:

$$V_f = 3.50 \times 10^{-4} P_o + 63.3\text{cc}, \tag{4.14}$$

where P_o is the tank pressure in Pa.

4.4.1 Uncertainty of Flow-Volume Measurements

The uncertainty of the volume measurement is estimated with the aid of expression (4.13) and is given by a standard uncertainty analysis [45]:

$$U_{V_f} = \left[\left(\frac{\partial V_s}{\partial \Delta P} U_{\Delta P} \right)^2 + \left(\frac{\partial V_s}{\partial P_{s,i}} U_{P_{s,i}} \right)^2 + \left(\frac{\partial V_s}{\partial \Delta V} U_{\Delta V} \right)^2 \right]^{\frac{1}{2}}, \tag{4.15}$$

where the $U_{\Delta P}$ is the uncertainty in ΔP (1.3×10^{-3} Pa), $U_{P_{s,i}}$ is the uncertainty in $P_{s,i}$ (7 Pa)[3] and $U_{\Delta V}$ is the uncertainty of ΔV ($\approx 1.3 \times 10^{-10}$ m^3). The dominant term in the volume uncertainty is the the third term due to the uncertainty of the change in volume associated with the syringe and the total uncertainty for the volume measurement is approximately ± 1 cc.

[3] The high-precision Setra was used in this experiment to measure $P_{s,i}$

4.5 Uncertainty Analysis of Mass Flow Measurement

The uncertainty in the mass flow measurement can be estimated with the aid of (4.9) and from the uncertainty in the slope of the differential pressure from the flow experiments(variable), temperature and volume measurements. The uncertainty can be shown to be:

$$U_{\dot{m}} = \left[\left(\frac{\partial \dot{m}}{\partial d\Delta P/dt} U_{d\Delta P/dt} \right)^2 + \left(\frac{\partial \dot{m}}{\partial V} U_V \right)^2 + \left(\frac{\partial \dot{m}}{\partial T} U_T \right)^2 \right]^{\frac{1}{2}}, \tag{4.16}$$

where $U_{d\Delta Pdt}$ is the uncertainty in the slope of the flow signal calculated from the least-squares curve fit described above ($\approx 1 \times 10^{-5}$ Pa/s), U_V is the uncertainty in the flow volume (≈ 1 cc), and U_T is the uncertainty in the measured temperature (0.01°C). The uncertainty for the mass flow measurement is dominated by the second term associated the volume measurement and is approximately 4×10^{-14} kg/s which is slightly larger than the estimated resolution reported above in section 4.3.2.

Chapter 5

Results and Discussion

The test conditions for the flow experiments are shown in Table 5.1 and each of the channels' flow history is given in appendix B. Throughout this thesis, it is assumed that the ideal equation of state adequately represents the state of the gas and the inlet and outlet pressures given in table 5.1 allow this assumption to be validated. To do so, the compressibility (a measure of the deviation from the ideal gas model) is calculated and it is shown in appendix A that the maximum deviation from ideality for CO_2 at all of the test conditions is $\leq 2\%$. For the other gases, the maximum deviations are $\leq .3\%$.

5.1 Flow Conductance

As discussed in section 2.2.2, the flow conductance ($\mathcal{C} = \frac{\dot{m}}{\Delta P}$) is used for validation of the Navier-Stokes equations before the normalized mass flow, along with the slip-flow model, is used to extract TMAC values. This model validation is essential because there is not a well-defined Knudsen number which can be used for flow-regime characterization. As an example of the use of the flow conductance for slip-flow validation, the measured flow conductance along with the least-squares fit to the data for argon exhausting to an outlet pressure of 13 kPa ($K_o = 0.41$) is shown in figure 5.1. The uncertainty bars represented in the figure are calculated using the definition of the flow conductance, the uncertainty in the mass flow and inlet and outlet pressures previously defined[1]. The data in figure 5.1 represents the "worst-case" (for the applicability of the slip-flow equations) of the argon flow conditions studied in this thesis. Although the outlet Knudsen number is significantly larger than that which is typically thought appropriate for the Navier-Stokes equations, it can be seen in the figure that the measured flow conductance is linear in mean pressure as the slip-flow model predicts. Furthermore, the comparison of the slope of the conductance derived from a least-squares fit to the data with the theoretical value is favorable, approximately .3% deviation. Thus the applicability of the Navier-Stokes analysis is demonstrated and the further use of the slip-flow expressions for TMAC extraction appears justified.

The fact that the Navier-Stokes equations appear to adequately model the flow in micromachined channels when the outlet Knudsen number is as large as 0.41 underscores our assertion that, when significant inlet-

[1] $U_{\mathcal{C}} = \left[\left(\frac{\partial \mathcal{C}}{\partial \dot{m}} U_{\dot{m}} \right)^2 + \left(\frac{\partial \mathcal{C}}{\partial P_i} U_{P_i} \right)^2 + \left(\frac{\partial \mathcal{C}}{\partial P_o} U_{P_o} \right)^2 \right]^{\frac{1}{2}}$ and is the expression used to calculate the uncertainty in the measured conductance shown in figure 5.1

Gas	Channel	P_i (kPa)	P_o (kPa)	K_o
argon	1A, 2A	≈130-430	≈ 13-102	≈ 0.05-0.41
N_2	1B	≈132-430	≈ 16-101	≈ 0.05-0.34
$C0_2$	1B	≈135-430	≈ 15-100	≈ 0.03-0.44

Table 5.1: Range of test conditions.

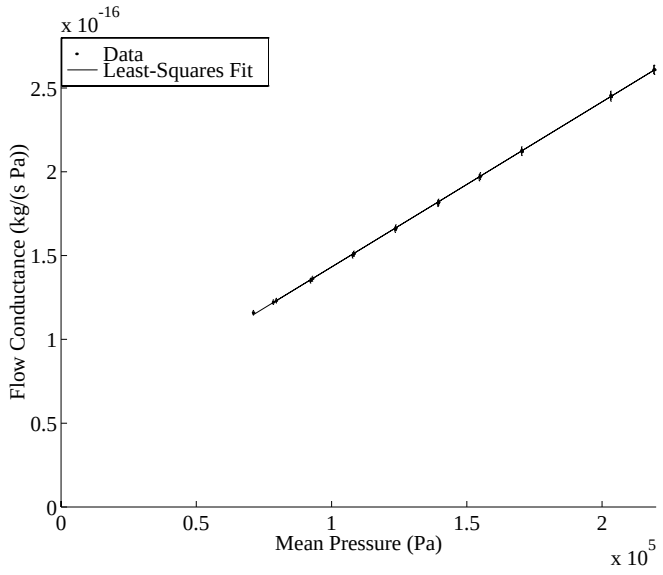

Figure 5.1: Flow conductance $\frac{\dot{m}}{\Delta P}$ as a function of mean pressure ($\bar{P}$) for argon exhausting to an outlet pressure of 13 kPa. The favorable comparison between the slope of the data obtained from the least-squares fit and the value calculated from equation (2.22) suggests that the Navier-Stokes model adequately describes the flow.

to-outlet pressure ratios are required to obtain measurable flow rates, the outlet Knudsen number may not be the most appropriate Knudsen number with which to characterize the flow regime.

Though the comparison of the slope from the flow conductance measurements can be used to validate the Navier-Stokes equations for the test conditions encountered in this thesis, we favor a slightly different form of comparison. To validate the slip-flow equations, we define an experimentally-determined viscosity which is derived from the slope of the flow conductance and compare its value to the viscosity used in the analysis to calculate the conductance. An obvious advantage of representing the comparison in the form of experimental and theoretical *viscosities* over experimental and theoretical *conductances*, is that the viscosity is independent of the channel geometric properties and is therefore conducive to comparison among various channels.

5.1.1 Experimentally-Determined Viscosity

If the channel is dimensionally stable (see appendix C), then the flow conductance can be used as a means for experimentally determining the gas viscosity. By a simple rearrangement of terms, the experimentally-determined gas viscosity can be shown to be:

$$\mu_{\mathrm{FV}} = \frac{H^3 w}{12 \mathcal{A} L R T}, \tag{5.1}$$

where $\mathcal{A}$ is the slope of the flow conductance versus mean pressure plot derived from a least-squares fit of the conductance data.

Uncertainty Analysis of Experimentally-Determined Viscosity

The uncertainty in the experimentally-determined viscosity is given by:

$$U_{\mu_{\mathrm{FV}}} = \left[\left(\frac{\partial \mu_{\mathrm{FV}}}{\partial H} U_H \right)^2 + \left(\frac{\partial \mu_{\mathrm{FV}}}{\partial w} U_w \right)^2 + \left(\frac{\partial \mu_{\mathrm{FV}}}{\partial \mathcal{A}} U_{\mathcal{A}} \right)^2 + \left(\frac{\partial \mu_{\mathrm{FV}}}{\partial L} U_L \right)^2 + \left(\frac{\partial \mu_{\mathrm{FV}}}{\partial T} U_T \right)^2 \right]^{\frac{1}{2}}, \tag{5.2}$$

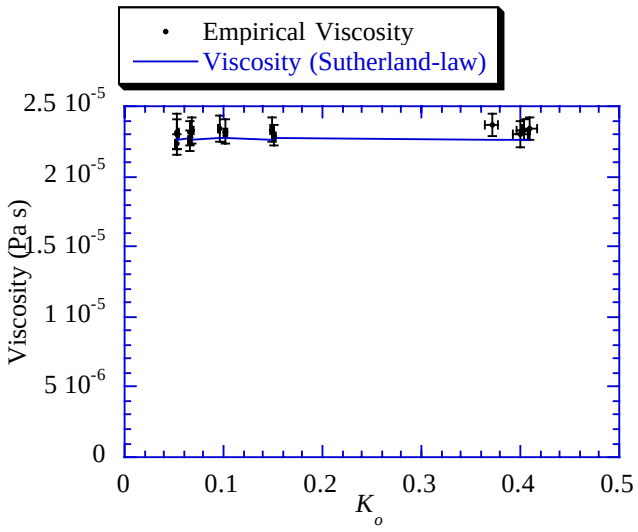

Figure 5.2: A comparison for argon in Channel 1A of the experimentally-determined viscosity to the values derived from the Sutherland-law formula. The data were compiled in both directions as the outlet Knudsen number was varied.

where μ_{FV} is given by equation (5.1). Each of the uncertainties is as given above and $U_{\mathcal{A}}$ is the standard deviation of the slope ($\approx 2 \times 10^{-23}$ kg/(s Pa^2)), calculated from the least-squares fit of the data. The dominant terms in the uncertainty of the experimentally-determined viscosity are due to the uncertainty in the channel height and width; the uncertainty in the experimentally-determined viscosity for the argon measurements is approximately 1×10^{-6} Pa s.

Plots of the experimentally-determined viscosities with the uncertainties calculated from equation (5.2) for argon, nitrogen and CO_2 as a function of outlet Knudsen number (K_o) are shown in figures 5.2, 5.3, 5.4 and 5.5.

Throughout the majority of the experiments the experimentally-determined viscosity is equal to the theoretical gas viscosity to within the uncertainty of the measurements, the exception clearly being the three points at the low outlet Knudsen numbers shown in figure 5.5. Based on the size of the outlet Knudsen number, the test conditions are well within the validity of the analysis yet, the comparison of the flow conductance (represented here in the form of viscosity) is not consistent with the theory. We believe that the most likely reason for this anomalous result is gas impurity introduced during the exchange of high-pressure gas tanks[2] but since records of tank changes were not kept, this belief can not be verified and the results can not be rejected. However, we have made a series of repeated measurements at $K_o = 0.032$ with CO_2 which act to confirm the belief that gas impurity was the cause of the above anomalous measurements. The results of the repeated CO_2 measurements are shown in figure 5.6

5.2 Normalized Flow and TMAC Measurements

The primary goal of this thesis is to use flow measurements within micromachined channels to derive values of the TMAC. In the previous section we have discussed the preliminary work which indicates the validity of the Navier Stokes equations for this purpose. Below we describe the procedure used to make the TMAC measurements and we present the results of our findings.

To extract a TMAC value from the flow results, the normalized mass flow ($\frac{\dot{m}}{P_i^2 - P_o^2}$) is plotted as a function

[2] During flow experiments a substantial amount of high-pressure gas is "consumed" by the pressure regulators i.e., bled to the atmosphere.

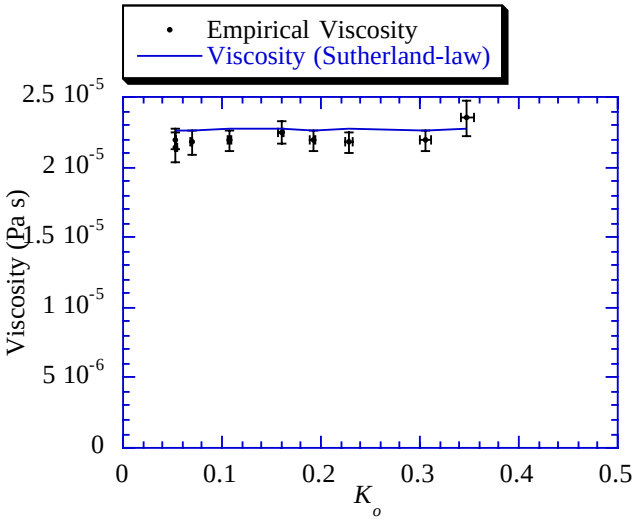

Figure 5.3: A comparison for argon flowing in Channel 2A of the experimentally-determined viscosity to the values derived from the Sutherland-law formula. The data were compiled in the direction from high to low Knudsen number.

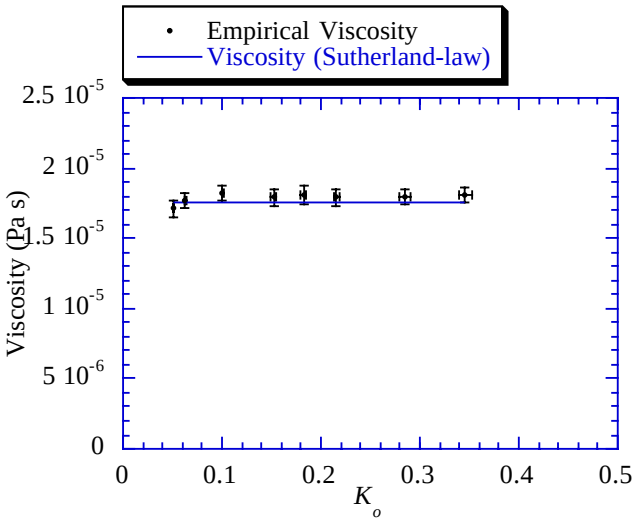

Figure 5.4: A comparison for N_2 flowing in Channel 1B of the experimentally-determined viscosity to the values derived from the Sutherland-law formula. The data were compiled in the direction from high to low Knudsen number.

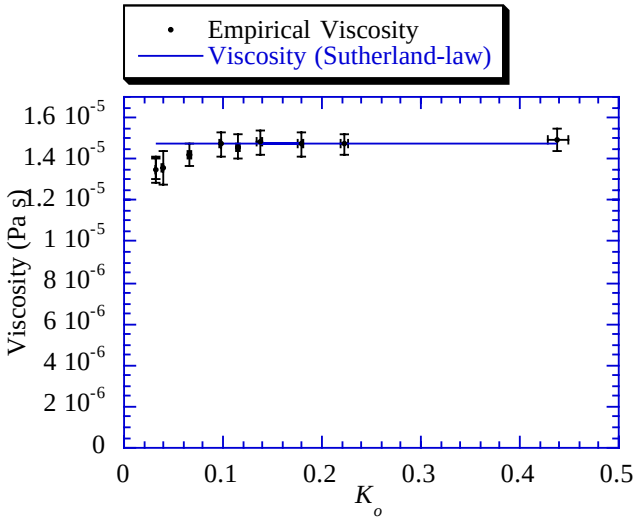

Figure 5.5: A comparison for CO_2 flowing in Channel 1B of the experimentally-determined viscosity to the values derived from the Sutherland-law. The data were compiled from high to low Knudsen number. Four data points near the low-end of the Knudsen number regime seem to indicate a discrepancy between the model and theory.

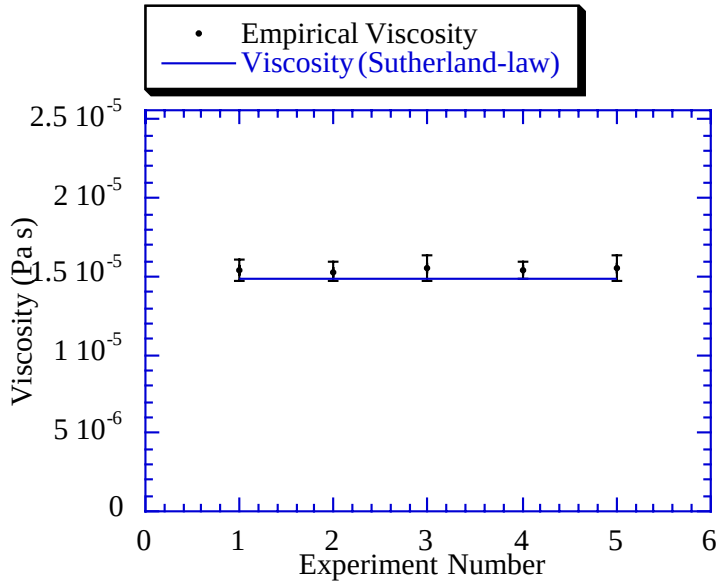

Figure 5.6: Experimentally-determined viscosity for a series of measurements made with CO_2 with $K_o = 0.03$.

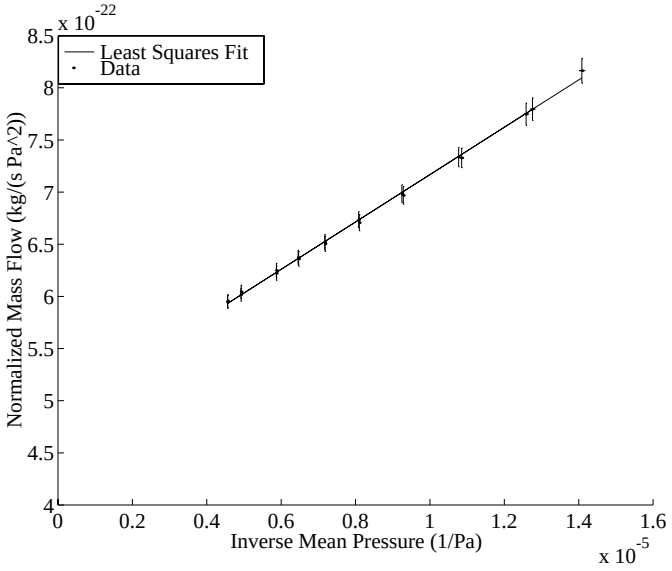

Figure 5.7: Data and least-squares fit (which is used to derive a value for the TMAC) for a representative set of argon flow experiments exhausting to an outlet pressure of 13 kPa.

of the inverse mean pressure $(\frac{2}{P_i+P_o})$[3]. If the normalized data is linear in the inverse mean pressure, then the slope of the normalized data can be used to extract a value for the TMAC by comparing it with the results of equation (2.24):

$$\text{TMAC} = \sigma_m = \frac{2}{\frac{2\mathcal{B}\mu LRT}{K_o P_o H^3 w} + 1}, \tag{5.3}$$

where $\frac{\mathcal{B}}{2}$ is the slope of the normalized data. A representative case for argon exhausting to an outlet pressure of 13 kPa is shown in figure 5.7. The uncertainty bars represented in the figure are calculated using the definition of the normalized mass flow and the uncertainty in the mass flow, inlet and outlet pressures previously defined. In this case, the coefficient of determination for the least-squares fit is better than .99 and for all of the TMAC results presented in this thesis the coefficient of determination is better than .96.

5.2.1 Uncertainty Analysis

The uncertainty for the value of the TMAC is given by:

$$\begin{aligned} U_{\text{TMAC}} = & \left[\left(\frac{\partial \sigma_m}{\partial \mathcal{B}/2} U_{\mathcal{B}/2} \right)^2 + \left(\frac{\partial \sigma_m}{\partial \mu} U_\mu \right)^2 + \left(\frac{\partial \sigma_m}{\partial L} U_L \right)^2 + \right. \\ & \left. \left(\frac{\partial \sigma_m}{\partial T} U_T \right)^2 + \left(\frac{\partial \sigma_m}{\partial H} U_H \right)^2 + \left(\frac{\partial \sigma_m}{\partial w} U_w \right)^2 \right]^{\frac{1}{2}}, \end{aligned} \tag{5.4}$$

where σ_m is given by (5.3) and $U_{\mathcal{B}/2}$ is given by the least-squares fit to the normalized data and is approximately 1×10^{-18} kg/(Pa s). The uncertainty bars presented below are calculated with equation (5.4) and the dominant terms are those due to the uncertainty in the channel height.

[3] Recall that the mean pressure is defined by the inlet and outlet pressure and, because the pressure variation along the channel is non-linear, the mean pressure thus defined does not represent the mean pressure within the channel.

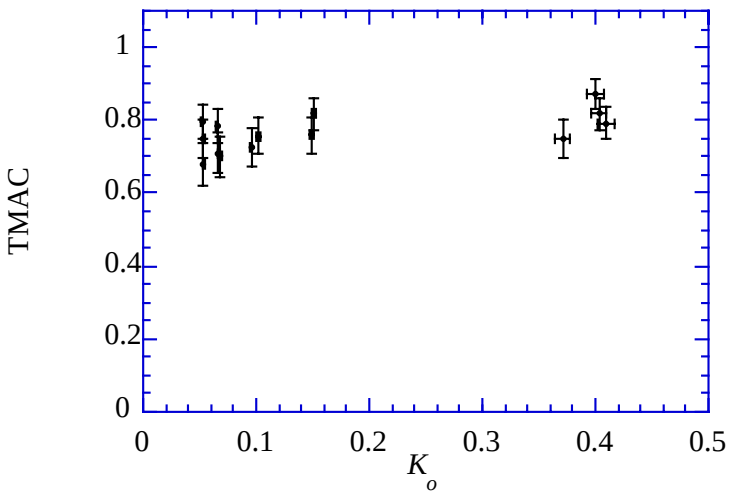

Figure 5.8: TMAC values for argon in Channel 1A. The data were compiled in the both directions starting from high to low Knudsen number.

5.3 TMAC as a function of K_o

A stated goal of this thesis is to measure the TMAC at various conditions encountered by state-of-the-art MEMS. In this section, we present TMAC measurements over a range of Knudsen numbers. The experimental results for argon, nitrogen and CO_2 are shown in figures 5.8, 5.9, 5.10 and 5.11. Each of the data points in these figures corresponds to a separate set of flow experiments similar to those shown in figure 5.7 and all of the results presented below coincide with the conductance comparisons shown in figures 5.2, 5.3, 5.4 and 5.5, respectively.

There are two striking features of the results. First, for the majority of the tests, there is a statistically significant deviation from unity of the TMAC value. Secondly, at values of the Knudsen number where the flow conductance indicated a discrepancy between the Navier-Stokes equations and the measurements, the TMAC values for CO_2 shown in figure 5.11 appear anomalous.

The numerical values of the TMAC for the low Knudsen number CO_2 data are greater than 1.2 and while TMAC values greater than unity have been reported as a result of a phenomenon known as net backscattering in which the gas molecules are preferentially reflected in the upstream direction, we do not believe that these results are indicative of this phenomenon. Instead, as discussed above, we believe that the results of the low Knudsen number CO_2 values are most likely a result of gas contamination and the TMAC values of the repeated CO_2 measurements corresponding to the viscosity plots shown in figure 5.6 seem to confirm this belief.

The fact that the TMAC is less than unity and appears to possess a value near 0.8 for all the gases and conditions of the tested channels is significant. It implies that the momentum exchanged between the impinging gas and the channel wall is not complete and that rebounding gas leaves the wall without having given up all its streamwise momentum to the surface i.e., it is not rebounded diffusely. This indicates that, to correctly model the exchange of momentum between MEMS and the fluids in which they are immersed with the slip-flow solutions of the Navier-Stokes equations, one may not be able to invoke the assumption of diffuse reflection. It also implies that numerical models which make use of this assumption may not be valid. In addition, the insensitivity to gas species indicates that the TMAC measured here may be an upper bound for this "untreated" surface and that, for specially treated surfaces, it may be possible to obtain values significantly lower.

Other interesting phenomena present in figures 5.9 and 5.10 is the apparent upturn in the TMAC taken as the outlet Knudsen number is decreased toward zero. The channels used in these tests (Channel 2A and Channel 1B) were pristine at the start of the tests and the direction of the tests was from high to low

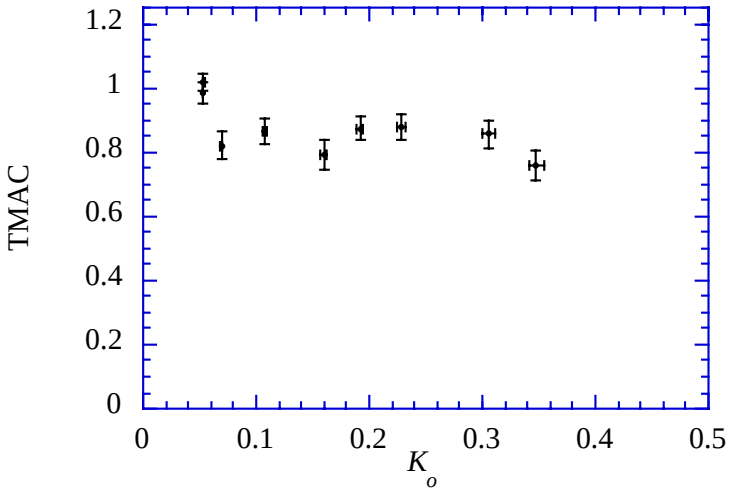

Figure 5.9: TMAC values for argon in Channel 2A. The data were compiled from high to low Knudsen number.

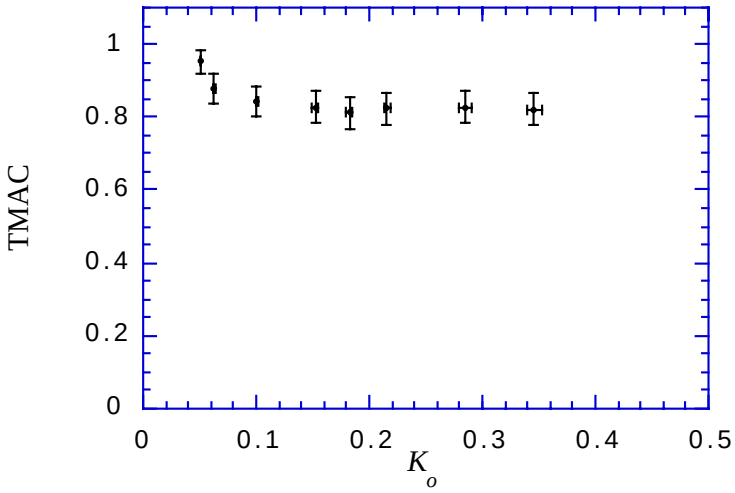

Figure 5.10: TMAC values for nitrogen in Channel 1B. The data were compiled from high to low Knudsen number.

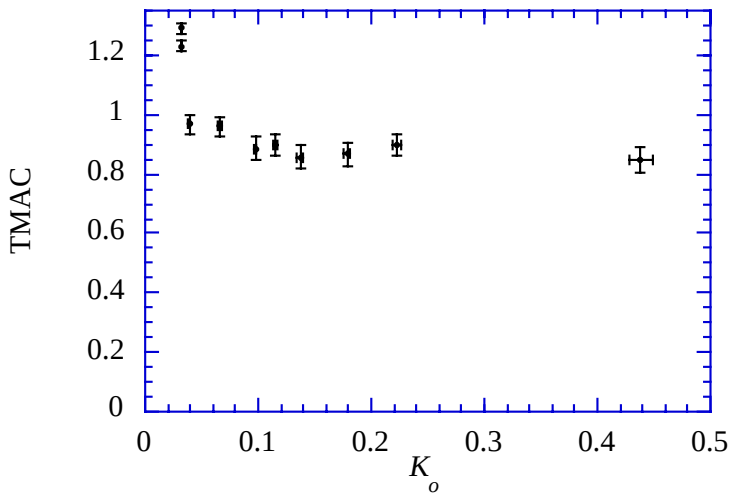

Figure 5.11: TMAC values for carbon dioxide in Channel 1A. The data were compiled from high to low Knudsen number.

Knudsen number. Therefore, by the experiments taken to derive the low Knudsen-number TMAC value, the channels had been exposed to approximately 140 separate flow experiments. It is unlikely that the up-turn is due to the fact that, at the start of the tests, the channels had never been exposed to the flow gas. Looking at the corresponding experimentally-determined viscosities, there is a slight down turn in the the case of N_2. However, in the case of argon, there is no corresponding shift in the experimentally-determined viscosity. Currently we have no explanation for the apparent up turn in the TMAC but would need more evidence in order to declare it physically meaningful.

5.4 Comparisons with other Microchannel Studies

An example of the data obtained in the flow studies conducted at UCLA is shown in figure 5.12. It is plotted in the flow conductance form based on the mass flow and pressure data provided by Chi-Ming Ho from the Center for Microsystems at UCLA [46]. The data are for a channel that is nominally 1.2 μm high, 40 μm wide and 4000 μm long, it consists of argon flow measurements exhausted to atmospheric pressure. This channel is identical to the channel discussed in Pong *et al.* [30], the cross-section of which is represented in figure 3.1.

The resolution of the mass flow measurements precludes the use of the slope of the flow conductance as a means of the Navier-Stokes model verification. However, if the slope of the least-squares fit to the data is compared to the theoretical value, there is approximately a 25% deviation between the least-squares and theoretical values. This is significant because the "capping" layer of the channel is a silicon nitride layer that is 1.2 μm thick (see figure 3.1). Even if the flow remains within the slip-flow regime, because of the cubic dependence of the mass flow pressure relationship, small variations in the height of the channel can significantly affect the mass flow rate. Variations in the channel height with pressure will also impact the pressure distribution along the channel length.

Like the use of the flow conductance for validation of the Navier-Stokes equation for microchannel flow, the use of the above normalization to extract meaningful values of the TMAC requires high-resolution mass flow measurements. In fact, the normalization for extracting the TMAC accentuates the need for high-resolution measurements. A plot of the normalized data derived from the mass flow and pressure results of the UCLA data is shown in figure 5.13

No statistically meaningful values for the TMAC can be extracted from these measurements.

Though the resolution of the mass flow measurements precludes the validity check of the slip-flow solution

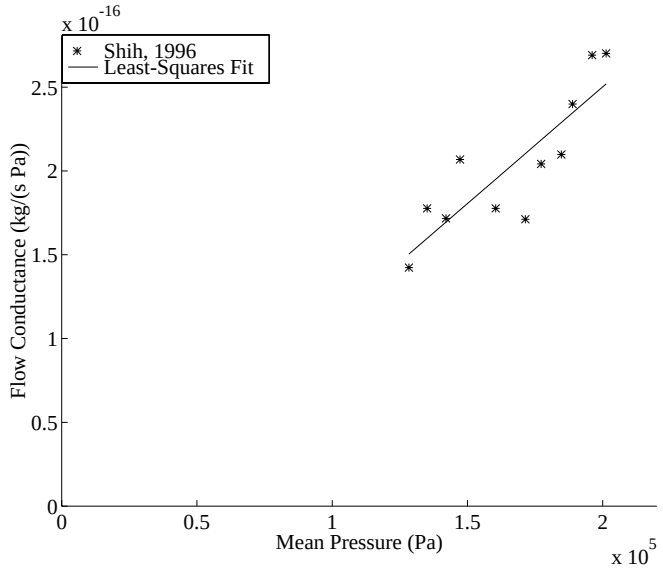

Figure 5.12: Flow conductance from Shih *et al.* as a function of mean pressure ($\bar{P}$) for argon exhausting to an atmospheric outlet pressure. The slope from the least-squares fit is approximately 25% larger than the value obtained with equation (2.22).

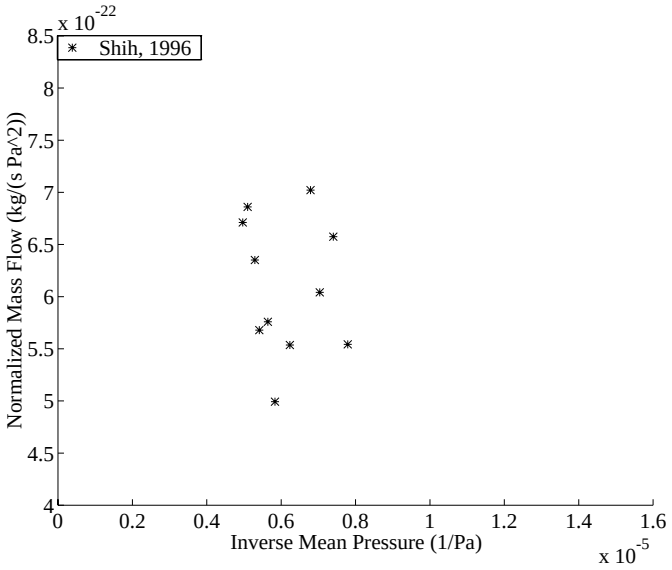

Figure 5.13: Normalized argon flow data from Shih *et al.* No statistically meaningful value for the TMAC can be extracted from this data

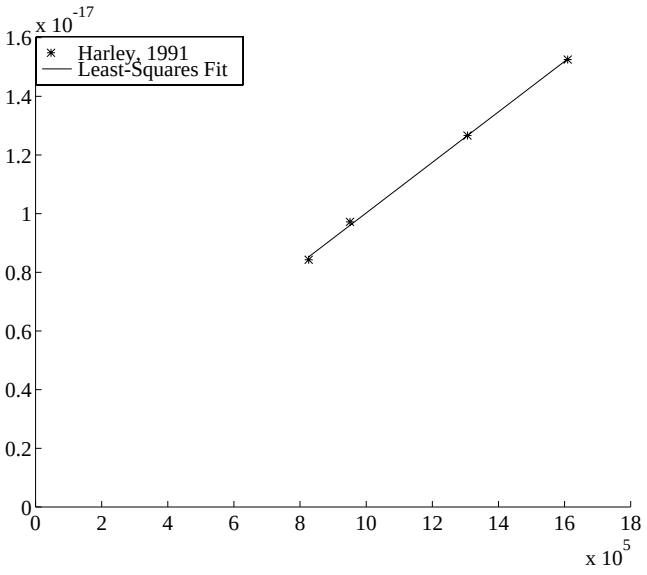

Figure 5.14: Flow conductance from Harley *et al.* as a function of mean pressure ($\bar{P}$) for helium exhausting to an atmospheric outlet pressure. The slope from the least-squares fit is approximately 5% larger than the value obtained with equation (2.22).

or the measurement of the effective TMAC[4], the UCLA group has the ability to measure the pressure distribution along the length of the channel. The reported results indicate that there can be a variation in the pressure distribution along the length of the channel which can not be explained by the slip-flow model [34]. Given the results in this thesis, which indicate that the *mass flow* can be accurately modeled with the slip-flow solution to the Navier-Stokes equations, these results are puzzling. However, it is possible that the channels themselves play a role in the anomalous pressure distribution data. For instance, if the 1.2 μm capping layer of silicon nitride is deflecting appreciably from the pressure within, the two-dimensional, constant-cross section model used in this analysis may no longer accurately portray the flow dynamics. Another possible explanation for the anomalous results attributable to a non-constant cross-section could be that the sacrificial PSG is not entirely removed prior to flow measurements.

The mass flow measurement for the UCLA work was conducted with a technique similar to that which was first utilized for flow measurements on micromachined channels by the UPenn group [36]. The technique is centered around timing the the advancement of a meniscus as the channel flow is exhausted into a calibrated capillary. For low-flow measurements, this technique is extremely sensitive to thermal fluctuations (which may be the cause of some of the variability in the UCLA data), but if the flow rates are sufficiently large to neglect the thermal noise, this technique is an effective means for measuring flow. Among their results, the UPenn group report on flows in micromachined channels that are exhausting to atmospheric pressure and have inlet to outlet pressure ratios of 15, 18, 25, 31 and mass flows of $1.2, 1.7, 3.0, 4.3 \times 10^{-11}$ kg/s. These flow rates are approximately an order of magnitude greater than the flow rates of the UCLA measurements.

An example of the data obtained in the flow studies conducted at UPenn is shown in figure 5.14. It is plotted in the flow conductance form based on the mass flow and pressure data provided by John Harley [47]. The data are for a channel that is nominally .51 μm high, 96.6 μm wide and 10.9 mm long, it consists of helium flow measurements exhausted to atmospheric pressure. The cross-section of the channel is represented schematically in figure 3.1. Though the data are too sparse for a statistically-significant comparison between the empirical and theoretical slope of the flow conductance, a comparison can still be made and it can be

[4] Because the channel top and bottom of the channel are not identical, the TMAC which is measured with the slip-flow normalization would only be the effective TMAC of the channel

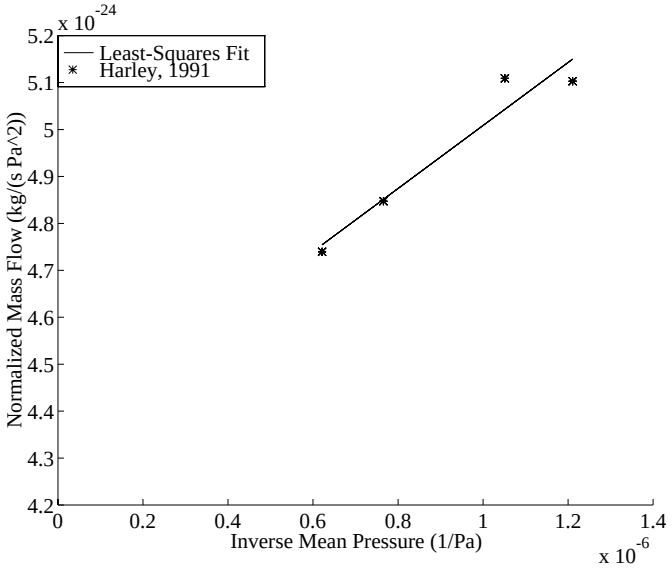

Figure 5.15: Normalized helium flow from Harley *et al.*. The sparseness of the data makes it difficult to extract statistically meaningful values of the TMAC.

shown that there is approximately a 5% variation between the data and model.

The UPenn data are also plotted in the normalized form used to extract values of the TMAC. This plot is shown in figure 5.15. The data is too sparse to derive a statistically-meaningful value of the TMAC. Nevertheless, the least squares fit is shown in the figure and the TMAC value derived from the least-squares fit is approximately 1.2. In addition to the sparsity of the data, the lack in the uncertainties of the reported channel dimensions precludes numerical bounds to be placed on the TMAC.

5.5 Deviations From Theory

We have shown that, with high-resolution flow measurements, the conductance comparison can be used to validate or *accept* the slip-flow equations for cases where the magnitude of the outlet Knudsen number would suggest that the Navier-Stokes equations are not valid. Given this result, an interesting question arises. Can the conductance comparison presented above also be used to *reject* flows in which the Navier-Stokes equations, with the given gas properties, no longer represent the flow? To investigate this, we have undertaken two sets of experiments. One set of experiments consisted of "extreme" flow conditions (Knudsen numbers) and another set consisted of measurements in which the gas was bubbled through water before entering the channel.

5.5.1 Extreme Knudsen Number

With helium exhausting to a pressure of 6.5 kPa, it is possible to obtain an outlet Knudsen number of 2.5 (well beyond the slip-flow regime). The inlet pressures for these tests (P_i) range from 133-413 kPa (K_i from .117 to .04), so a significant portion of the channel length lies beyond the validity of the slip-flow approximation. A plot of the conductance for these conditions is shown in figure 5.16. There are several interesting points to this data. To begin, the data are "noisier" than the previous experiments. Secondly, there is a slight curvature to the measured flow conductance which is not predicted by the slip-flow model. Finally, if a linear least-squares model is fitted to the data, the slope of the measured flow conductance is approximately 11% greater than the slope of the conductance calculated with the theory. This suggests that the Navier-Stokes model overestimates the momentum exchange between the fluid and the channel and

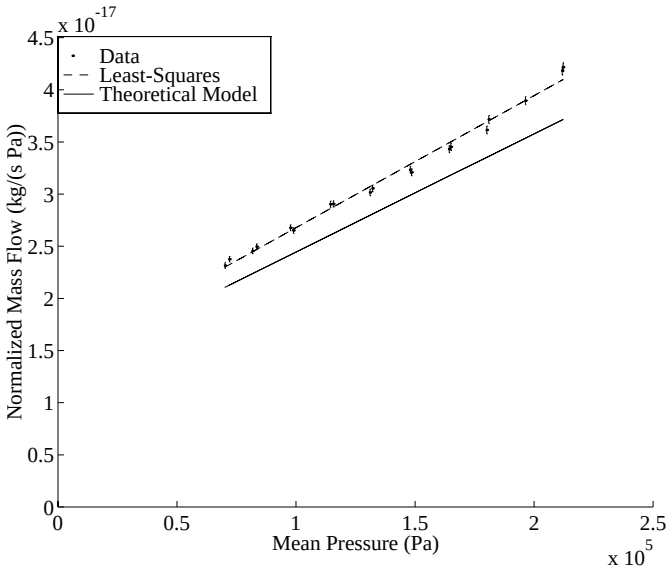

Figure 5.16: Flow conductance $\frac{\dot{m}}{\Delta P}$ as a function of mean pressure $\bar{P}$ for helium exhausting to an outlet pressure of 6.5 kPa, $K_o = 2.5$ and the Navier-Stokes model clearly underestimates the magnitude of the flow conductance and therefore is shown not to be valid for this test condition.

this aspect of a decrease in the momentum exchanged is consistent with our understanding of the effects of increased rarefaction.

The apparent breakdown in the slip-flow expressions indicates that the flow conductance *may* be used to reject experimental conditions that present flows beyond the valid range of the Navier-Stokes equations. However, more work is definitely needed in the area of determining the breakdown of the slip-flow model. For instance, the mass flows used to derive the flow conductance values for this set of experiments were measured at tank (or system) pressures of 6.5 kPa. This tank pressure is well below the tank pressure at which the system volume was calibrated (see section 4.4).

Because there is an 11% discrepancy between the slope of the measured and the theoretical flow conductances, the use of the mass flow normalization presented above for the purposes of TMAC extraction is precluded. However, the normalized mass flow which is used above to extract the TMAC can still be plotted (see figure 5.17). The data in figure 5.17 is not linear in inverse mean pressure. This can be taken as further evidence of the breakdown of the slip-flow expressions to adequately represent the flow.

If the slip-flow solution to the Navier-Stokes equations fail to adequately represent the flow for the conditions of the data in figure 5.16, then the equation for the pressure distribution (2.20) may no longer accurately represent the pressure distribution within the channel. Therefore, the pressure within the channel and thus Knudsen number remains unknown. However, if the trend represented in figure 2.2 of decreasing curvature with increasing rarefaction of the pressure versus length plot continues as the Navier-Stokes equations cease to be valid, then this would be further evidence that a more substantial length (than would be predicted by equation (2.20)) of the channel falls beyond the region where slip-flow is applicable.

5.5.2 Effects of Water Vapor

To investigate the effects that water vapor has on the exchange of momentum and the TMAC, a test that consisted of fourteen separate sets of flow experiments was conducted. The fourteen separate sets were split into three groups: dry flow, hydrated flow and post-hydrated dry flow. To begin, a series of seven separate sets of measurements were made on Channel 2A with desiccated argon (these dry flow measurements were identical to the previous experiments) After, three sets of measurements were made with argon that was bubbled through a water bath before entering the channel (hydrated flow). Finally, four sets of measurements

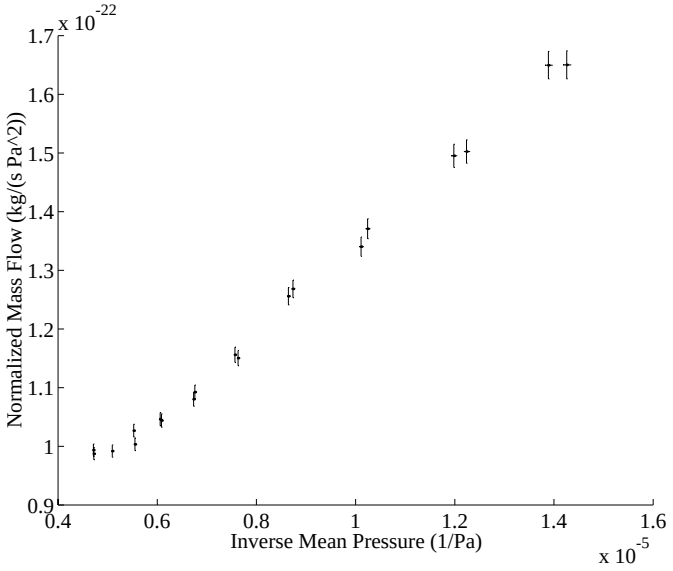

Figure 5.17: Normalized flow $\frac{\dot{m}}{P_i^2 - P_o^2}$ as a function of inverse mean pressure $1/\bar{P}$ for helium exhausting to an outlet pressure of 6.5 kPa, $K_o = 2.5$. The slip-flow model predicts that the normalized flow should be linear in inverse mean pressure, the data shows that it is not.

were made on argon where the water bath was removed and the argon passed through a desiccant (post-hydrated dry flow). Throughout the tests the outlet pressure was set to atmospheric pressure and $K_o = 0.05$. The results of the viscosity comparison for this set of experiments is shown in figure 5.18. Immediately after the argon was bubbled through the water, there is a significant shift in the experimentally-determined viscosity. Once the hydration is removed, the experimentally-determined viscosity appears to return to it pre-hydration level.

We can investigate more closely the data from the "hydrated" experiments by looking at the flow conductance from, for example, experiment #9 in figure 5.18. Such a comparison is shown in figure 5.19. There is a clear discrepancy between the measured flow conductance and the theoretical flow conductance. One conclusion which can be drawn from this comparison is that water which is entrained as the argon is bubbled through the bath alters the gas properties perhaps to the extent that the gas can no longer be modeled as ideal. Another interesting aspect of the comparison is that at a mean pressure of 180 kPa the empirical flow conductance and model coincide. We have no plausible explanation for this result but it should be noted that point at which the empirical flow conductance and model coincide will depend on the value of the TMAC used to plot the theoretical flow conductance, i.e., the intercept of the theoretical conductance. In this case of figure 5.19 the "dry" value of the TMAC (0.8) was used to plot the theoretical model.

If we look at the normalization used for extracting the TMAC for experiment # 9 (figure 5.20), we see an extreme deviation from the model. The slip-flow model suggests that the normalized flow should be linear in inverse pressure; for the case of the "wet" data shown in figure 5.20 it clearly is not linear. This could be the result of several phenomena but we believe the most likely cause is a deviation from the ideal gas law associated with the entrained water vapor. Regardless of the cause, it is clear that the normalized flow results can not be used to extract reasonable values for the TMAC. However, as soon as the water bath is removed and the argon is desiccated, the normalized flow results returned to a linear function of the inverse mean pressure and so the TMAC could be derived for the post-hydration flow results. The results of the post-hydration tests are included in figure 5.21. After the hydration was removed, there appears to be a jump in the value of the TMAC from a pre-hydration value of near 0.8 to a post-hydration value of near 1 before it seems to settle back to return to a value near 0.8. Unfortunately the test was terminated before it was clear if the TMAC value was truly settling to a value near 0.8.

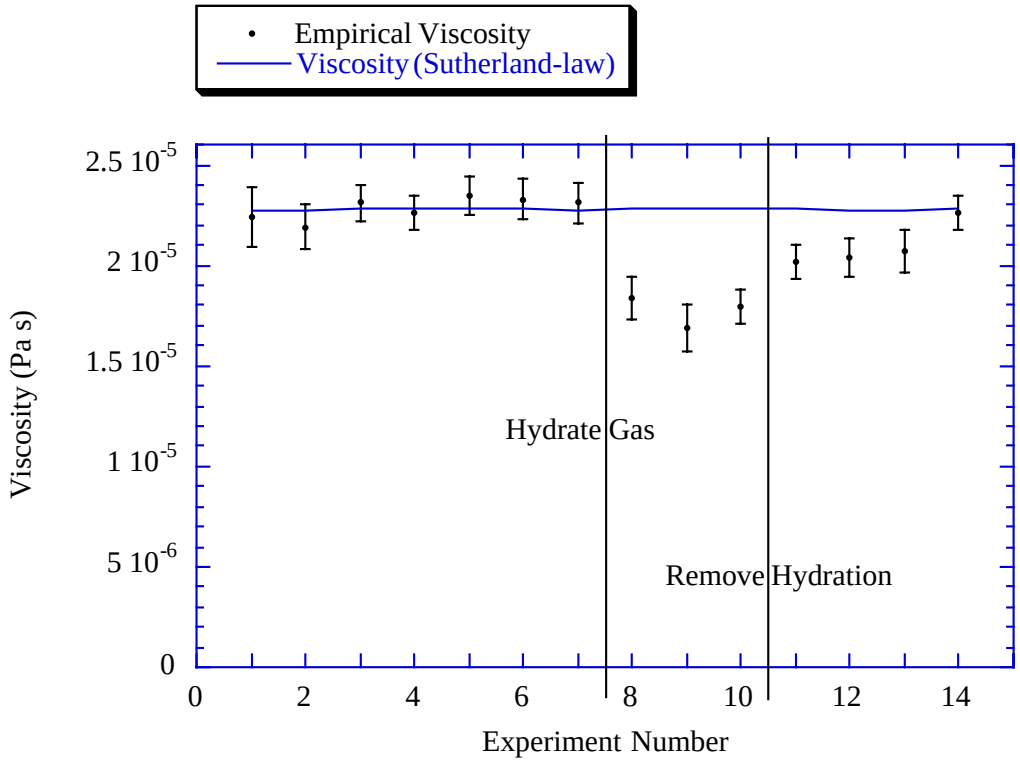

Figure 5.18: Comparison of the experimentally-determined viscosity to the theoretical viscosity for a set of tests designed to investigate the effects of water vapor. After experiment 7, the argon was bubbled through a water bath before entering the channel. After experiment 10, the argon was passed through a desiccant before entering the channel. Clearly once the argon is bubbled through the water, the experimentally-determined viscosity decreases. When the water bath is removed and the argon is desiccated again, it appears as the though it takes several test runs for the experimentally-determined viscosity to return to it's previous "dry" value

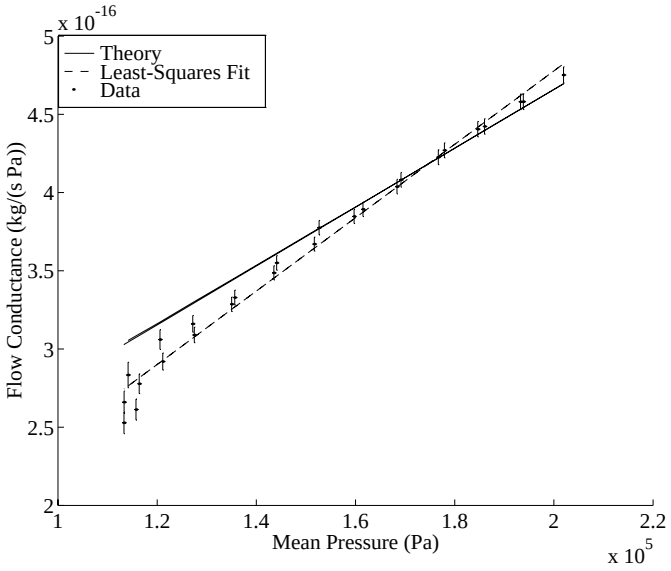

Figure 5.19: Flow conductance from an experiment in which argon was first bubbled through a water bath before being introduced into the channel. The mismatch between the calculated and measured flow conductance indicates a breakdown of the Navier-Stokes equations or, at least, a variation in gas properties associated an increase in the water content of the gas.

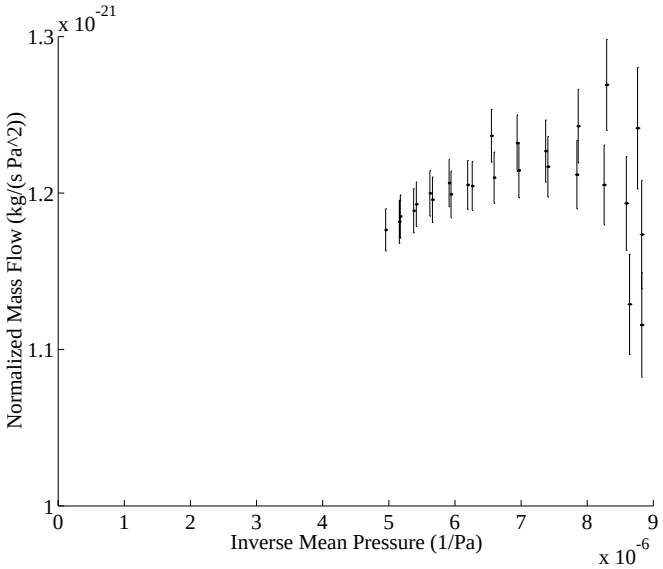

Figure 5.20: Normalized flow which clearly shows the non-linear aspect of the data; no reasonable TMAC can be extracted from these results

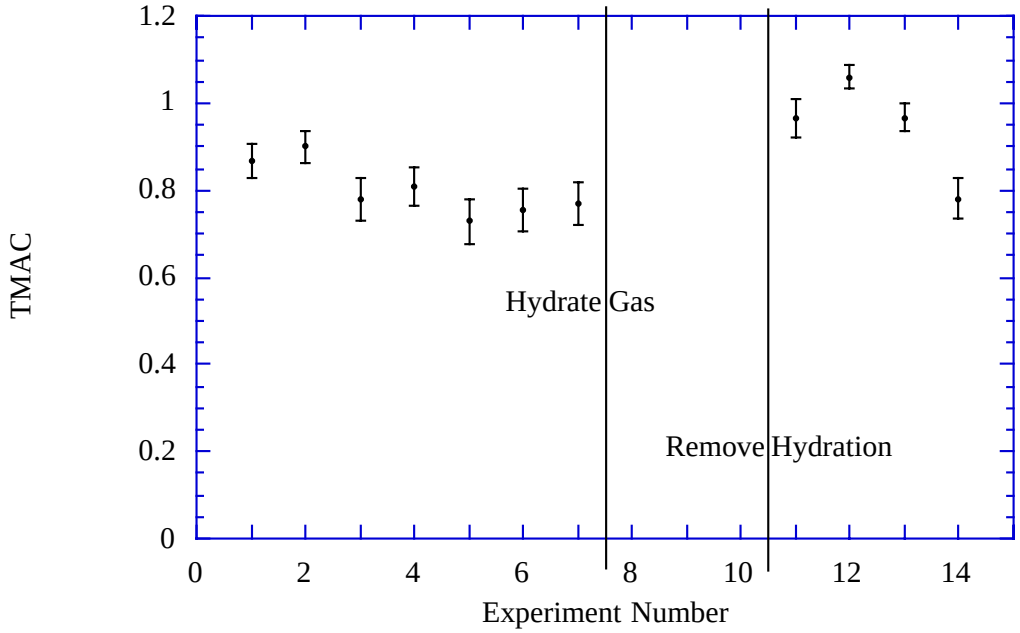

Figure 5.21: The TMAC could not be defined for experiment #s 8,9, or 10. However, it appears as though the effects of entrained water vapor are to increase the TMAC (experiments 11,12 and 13) and that this effect is reversible.

Chapter 6

Conclusions

The dynamics of the interactions of MEMS with their surrounding gas can exhibit the effects of compressibility and rarefaction while simultaneously possessing low characteristic Reynolds numbers. Furthermore, MEMS are often designed as dynamic systems and possess complex three-dimensional geometries of unique materials. Together, these attributes highlight the unique aspect of the momentum exchanged between MEMS and their surroundings. A compressible gas in an unsteady, low-Reynolds number regime interacting with molecularly-smooth surfaces in the presence of rarefaction is a unique situation not often encountered. Yet, this is the situation that the designers of high-performance MEMS are faced with.

In this thesis, we have focussed on the aspect of the problem associated with the gas interaction with the molecularly smooth surface in the presence of rarefaction but, in so doing, have also elucidated other aspect of micro fluid mechanics including the impact of low characteristic Reynolds number and gas compressibility. By undertaking a theoretical and experimental investigation on compressible gas flow through simple two-dimensional channels, we have simplified the situation that is facing the designers of high-performance MEMS somewhat by not addressing the unsteady aspect or the effects of complex geometry. However, we have used this steady-flow situation as a means of deriving a numerical value of the TMAC near 0.8 which will be an important component for future studies in these more complex situations.

In this study, we have found that the TMAC is independent of the outlet Knudsen number for the cases tested and that the outlet Knudsen number may not adequately represent the flow when it comes to regime characterization. Furthermore, we have found that the TMAC is independent of the gas species for the gases discussed in this thesis. It remains to be seen what impact, if any, the surface material has upon the value of the TMAC.

6.1 Impact upon MEMS

Current MEMS operated at atmospheric pressure can easily exhibit rarefied phenomenon. When rarefaction is present, the extent to which gas molecules accommodate to the surface plays an important role in determining the system dynamics. A reduction in the extent of accommodation which, for the case of tangential momentum is reflected in the reduction of the numerical value of the TMAC, acts to further accentuate the significance of rarefied phenomena. For example, a 20% reduction in the value of the TMAC from unity to 0.8 can increase the value of the slip velocity at the wall by 50%.

To model the significance of the impact that slip-flow has upon the dynamics of MEMS, researchers have undertaken computational investigations into "parallel-plate squeeze-type devices" [4]. These types of devices are commonly utilized in micromachined accelerometers, and have such applications as triggers for air-bag deployment in automobiles. Therefore, the dynamic response to impulsive forces of such devices is of interest to the MEMS designer and an example of the impact that slip-flow can have upon the modeled dynamic response of a typical "parallel-plate squeeze-type" device is shown in figure 6.1. The exact configuration and numerical model is given in Chen and Yao [4], but the initial gap spacing is 5μm and the surrounding gas is assumed to possess the standard properties of air at atmospheric pressure. The system damping is modeled with the Reynolds equation for squeeze film and the slip-flow boundary condition is imposed. The

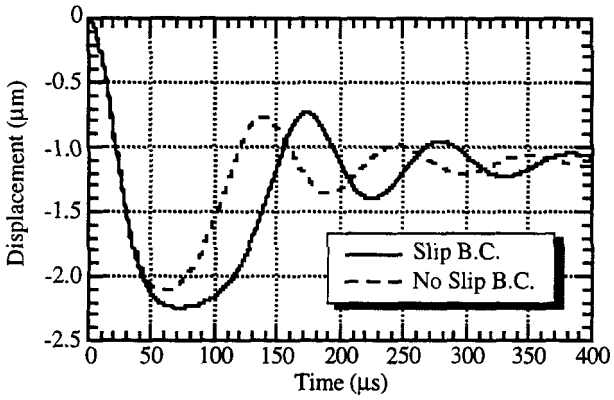

Figure 6.1: The dynamic response to an impulse for an underdamped micromachined "parallel-plate squeeze-type" device from Chen and Yao [4].

tangential momentum accommodation coefficient is assumed to be equal to 0.9. As demonstrated by the results of the model for the dynamic response to an impulsive force shown in figure 6.1, the effect of slip flow and, by extension the value of the TMAC, can be shown to have a significant impact on the dynamic response of a micromachined system.

6.2 Contributions of this Thesis

In this thesis, we have developed a mass flow measurement system, a micromachined channel and an analytic framework for interpreting microchannel flow results in a manner that is conducive to TMAC measurement. The resolution of the mass flow hardware rivals that of state-of-the-art vacuum leak-checking systems, but operates at pressures near atmospheric. The channel fabrication procedure which has been developed has proven to be a robust means with which to fabricate channels that are well-suited to the needs of this study (tight dimensional control, identical surface structure and stiff mechanical properties). Also the fabrication sequence is sufficiently general such that a broad range of materials could be coated within the channels and tested.

With the combination of these three contributions (mass flow system, channel fabrication and analytical framework), we have shown that values of the TMAC for single-crystal silicon upon which a native oxide resides for the gases argon, nitrogen and carbon dioxide can have statistically meaningful values that are less than unity. The value seems to be independent of Knudsen number for the cases tested and appears to range between 0.75 and 0.85. It has been shown that the water vapor seems to effect the TMAC by increasing it value to near unity and it appears as though this effect is reversible.

6.3 Recommendations for Future Work

We have demonstrated that TMAC values of less than unity can exist for prime silicon upon which a native oxide resides but we can not generalize this finding to other surfaces. MEMS possess a wide variety of materials and, due to the varied and extensive chemical processing associated with various systems, surface chemical composition. Therefore, we believe that future work on gaseous flow in micromachined channels should include studies on the impact that surface properties have upon the TMAC.

Another interesting component of future studies will include a detailed assessment of when the slip-flow model ceases to adequately represent the flow dynamics in micromachined channels. This could be undertaken with a series of measurements at various inlet and outlet pressures with helium. Finally, the photolithographic techniques employed in this thesis allow for a wide variety of internal-flow geometries, including nozzles, diffusers and orifices and one can envision many uses for such devices.

Appendix A

Gas Properties

The values of the gas properties used in this thesis are given in Table A.1

Values of viscosity used in this thesis for comparative purposes are derived from the Sutherland-law formulation. The Sutherland-law for viscosity is given by [35]:

$$\mu \approx \mu_0 \left(\frac{T}{T_0}\right)^{\frac{3}{2}} \frac{T_o + S}{T + S}, \tag{A.1}$$

where T is the temperature and T_0, μ_0 and S are constants gas-specific constants. For the gases used in this thesis, the constants are shown in Table A.2 [50].

In order to verify that the ideal equation of state accurately models the gas used for the flow tests, we can calculate the compressibility of the gas defined as:

$$Z = \frac{P}{P_{BB}}, \tag{A.2}$$

where P is the measured pressure and P_{BB} is the pressure calculated using the Beattie-Bridgeman equation of state state [6]:

$$P_{BB} = \frac{RT(1-C)}{v^2}(v + B) - \frac{A}{v^2}, \tag{A.3}$$

where R is the ideal gas constant, T is the temperature, $A = A_0(1 - a/v)$, $B = B_0(1 - b/v)$, $C = C_0/vT^3$ and A_0, a, B_0, b and C_0 are gas-specific constants. The value of v used in (A.3) is calculated using the ideal equation of state. The relevant gas constants constants are given in Table A.3 [6]. For all the tests the variation from ideality of the gas was less than 2%.

Gas	$\mathcal{R}$ (J/(kg K))	σ (m)	γ	μ (Pa s)
argon	208.1 [48]	360×10^{-12} [49]	1.67 [48]	22.6×10^{-6}
N_2	296.8 [48]	370×10^{-12} [49]	1.40 [48]	17.6×10^{-6}
$C0_2$	188.9 [48]	460×10^{-12} [49]	1.30 [48]	14.7×10^{-6}
helium	2077 [48]	210×10^{-12} [49]	1.67 [48]	19.7×10^{-6}

Table A.1: Relevant gas constants.

Gas	T_0 (K)	μ_0 (Pa s)	S (K)
argon	273	21.25×10^{-6}	144
N_2	273	16.63×10^{-6}	107
$C0_2$	273	13.7×10^{-6}	222
helium	273	18.7×10^{-6}	79

Table A.2: Sutherland-law parameters for selected gases.

Gas	A_0	a	B_0	b	$10^{-4}C_0$
argon	130.78	0.02328	0.03931	0.0	5.99
N_2	136.23	0.02617	0.10476	-.00691	4.20
$C0_2$	507.28	0.07132	0.05046	0.07235	66.0
helium	2.1888	0.05984	0.01400	0.0	0.0040

Table A.3: Gas constants for Beattie-Bridgeman equation of state (Pressure in kPa, specific volume in m^3/kmol)

Gas	Max Pressure (kPa)	compressibility
argon	460	1.002
N_2	430	1.001
$C0_2$	430	1.017
helium	413	0.997

Table A.4: Gas compressibility at maximum test pressure

Appendix B

Channel History

In this thesis three separate channels were tested: Channel 1A, Channel1B, Channel 2A. Below, a description of the history of each of the channels is given.

B.1 Channel 1A

Channel 1A was bonded on 4/9/94 and diced on 4/10/94. Many hundred flow tests with helium and argon were conducted on Channel 1A for system debugging between 4/10/94 and 12/17/95 when the first recorded flow results were acquired.

B.2 Channel 1B

Channel 1B was completed at the same time as Channel 1A but was not tested until the first nitrogen tests which began on 4/1/96. Subsequent to the nitrogen tests, CO_2 was tested from 4/22/96 to 5/3/96.

B.3 Channel 2A

Channel 2A was completed with the modified mask set on 6/11/96 and diced on 6/12/96. Argon flow tests began 6/12/96 and ran through to 6/24/96. The hydrated experiments were run on Channel 2A over a period from 10/1/96 to 10/18/96.

Appendix C

Channel Deflection

To estimate the deflection of the capping wafer due to the pressure within the channel, the capping wafer can be modeled as a rectangular plate that is simply supported at the channel inlet and outlet and is fixed along the channel length (see figure C.1). It is further assumed that the pressure within the channel is uniform. The assumption of uniform pressure within the channel is obviously a gross simplification but is conservative in the sense that the deflection will be over-estimated. With these assumptions, it can be shown that the maximum deflection for a high aspect ratio plate $L/W >> 1$ due to uniform pressure within the channel is given by [51]

$$h_{max} \approx 0.00260 \frac{12 P w^4 (1-\nu^2)}{E t^3} \tag{C.1}$$

where P is the *gauge* pressure within the channel, w is the channel width, E is Young's modulus (taken as 163 GPa), t is the capping wafer thickness and ν is Poisson's ratio (taken as .223). For the case of Channel 2A, in which the gauge pressure within the channel is 360 kPa, the model predicts a maximum channel deflection less than 8×10^{-14}m at least 5 orders of magnitude less than the uncertainty in channel height.

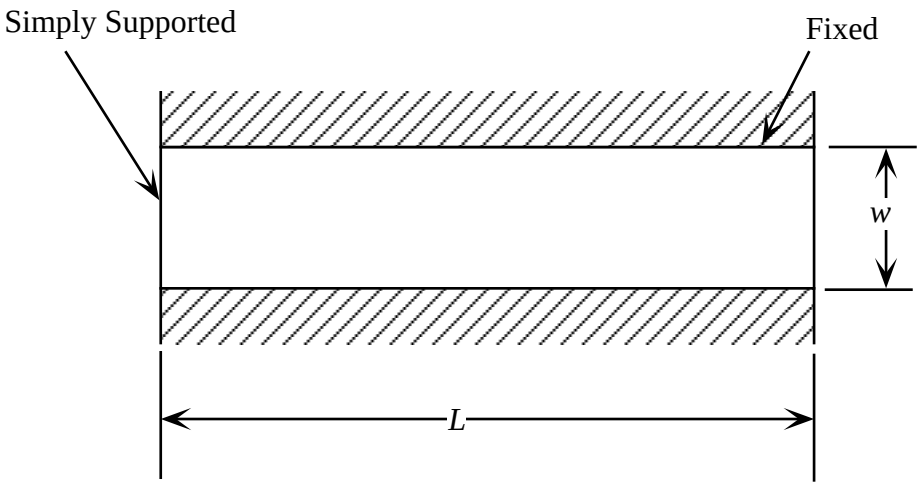

Figure C.1: Schematic representation of the capping wafer and boundary condition used to estimate the deflection of the channel due to the pressure within the channel

Appendix D

Dual-Tank Flow System

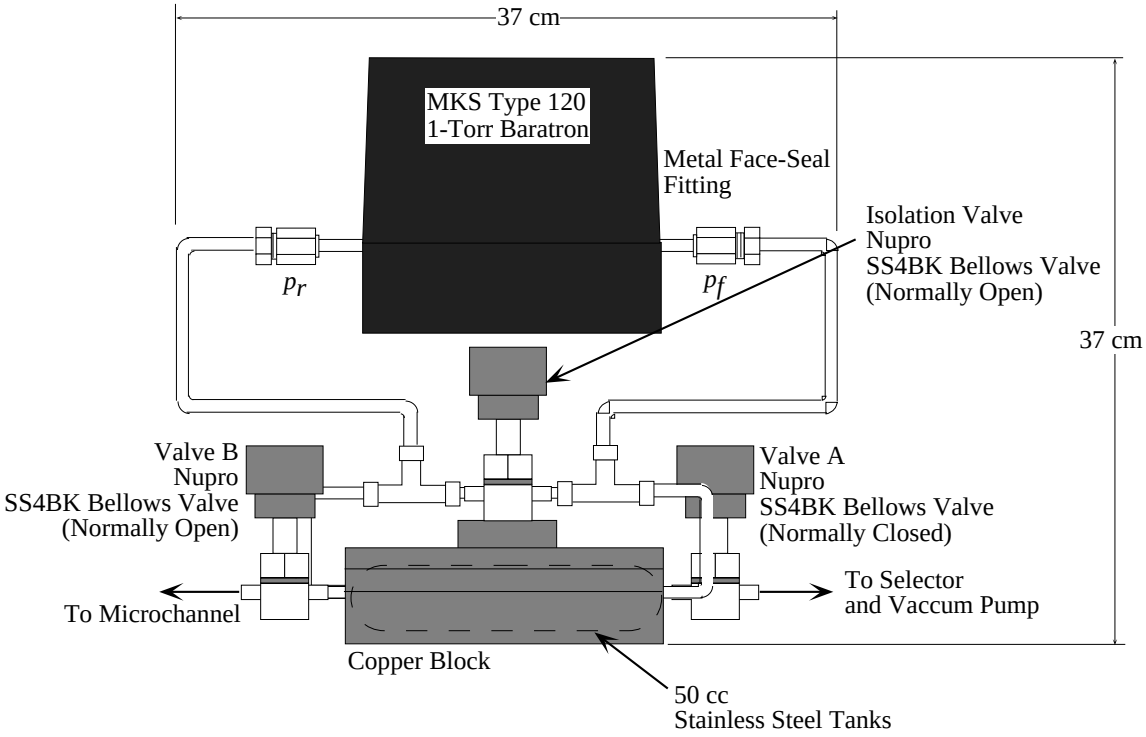

Figure D.1: Dual-tank flow system and primary system components.

Appendix E

Masks

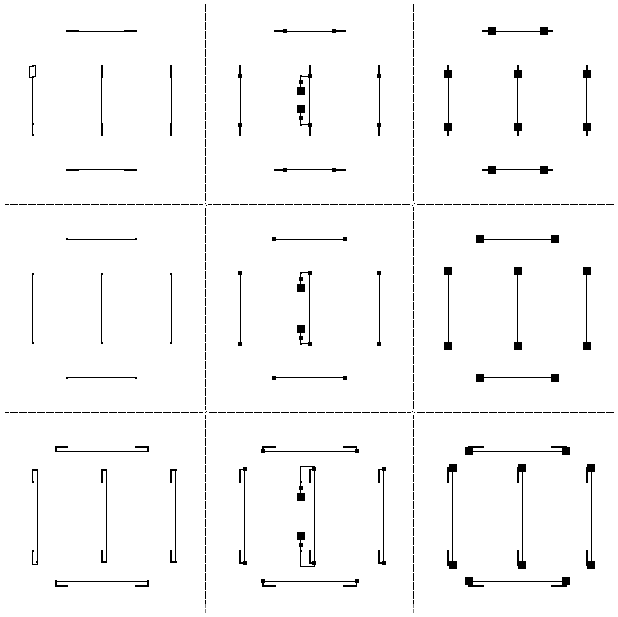

Figure E.1: Mask for Channel 1.

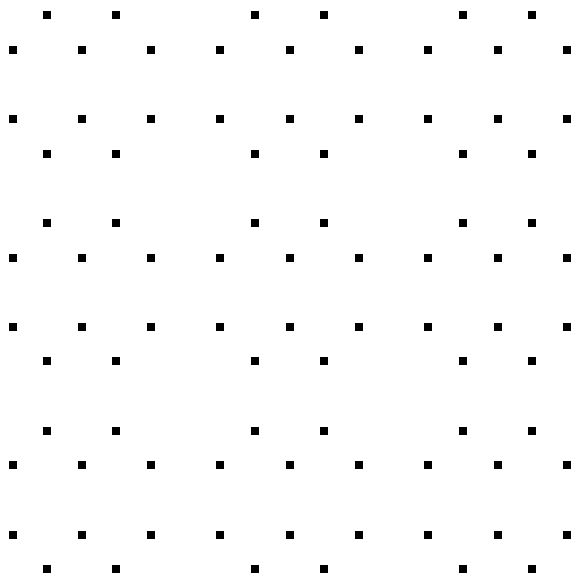

Figure E.2: Mask for backside access ports, used for Channel 1 and Channel 2.

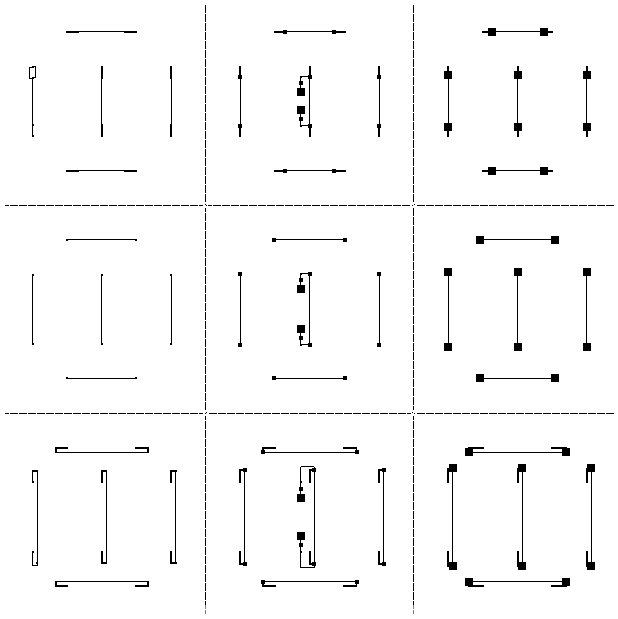

Figure E.3: Mask for Channel 2.

Appendix F

Process Traveler

PROCESS TRAVELER

MICROCHANNEL FABRICATION

LOT

LOT OWNER Errol Arkilic

STEP	STEP DESCRIPTION	STATUS	
CHANNEL WAFER Starting material : double polished n-type <100> .5-2Ωcm			
1	Oxidation dox13.3k.set (ICL)	Number wafers Opset start Opset finish	_____ _____ _____
2	Photolithography Mask 1 (TRL)	Number wafers Opset start Opset finish	_____ _____ _____
3	Pattern Oxide wox13.3k.set (TRL)	Number wafers Opset start Opset finish	_____ _____ _____
4	Photoresist Strip Piranha 10 minutes (ICL)	Number wafers Opset start Opset finish	_____ _____ _____
5	Silicon Nitride Coverage (ICL)	Number wafers Opset start Opset finish	_____ _____ _____
6	Back Side Photolithography Mask 2 (TRL)	Number wafers Opset start Opset finish	_____ _____ _____
7	Plasma Etch Port Openings	Number wafers	_____

	recipe 13	Opset start	_____
	45 seconds (ICL)	Opset finish	_____
8	Photoresist Strip	Number wafers	_____
	Piranha	Opset start	_____
	10 minutes (ICL)	Opset finish	_____
9	KOH etch	Number wafers	_____
	20 % KOH, 56 °C	Opset start	_____
	28 Hrs (RGL)	Opset finish	_____
10	Post KOH clean	Number wafers	_____
	(RGL)	Opset start	_____
	(TRL)	Opset finish	_____

CAPPING WAFER
Starting material : double polished n-type <100> 10-20Ωcm

BONDED CHANNEL WAFER
Starting material : Channel Wafer & Capping Wafer

1	Bond Wafers	Number wafers	_____
	(dbonding.set)	Opset start	_____
	(ICL)	Opset finish	_____

END

Bibliography

[1] M. Andrews, I. Harris, and G. Tuner. A comparison of squeeze-film theory with measurements on a microstructure. *Sensors and Actuators*, (36):79–87, 1993.

[2] H. Hosaka, K. Itao, and S. Kuroda. Damping characteristics of beam-shaped micro-oscillators. *Sensors and Actuators*, (49):87–95, 1995.

[3] Mitchell Novack. Design and fabrication of a thin film micromachined acccelerometer. Master's thesis, Massachusetts Institute of Technology, Cambridge, MA, September 1992.

[4] C.L. Chen and Yao J.J. Damping control of mems devices using structural design approach. In *Solid State Sensor and Actuator Workshop*, pages 72–75, Hilton Head, June 1996.

[5] W. Steckelmacher. Knudsen flow 75 years on: the current state of the art for flow of rarefied gases in tubes. *Rep. Prog. Phys.*, (49:1083-1107), 1986.

[6] R.E. Sonntag and G.J. Van Wylen. *Introduction to Thermodynamics: Classical and Statistical*. John Wiley and Sons, New York, 1982.

[7] S.A. Schaff and P.L. Chambre. Flow of Rarefied Gases. In *Fundamentals of Gas Dynamics*, chapter H. Princeton University Press, New Jersey, 1958.

[8] X. Zhong. On numerical solutions of the Burnett equations for the hypersonic flow past 2-d circular blunt leading edges in continuum transition regime. (AIAA 93-3092), 1993.

[9] K.A Comeaux, Chapman. D.R., and R.W. MacCormack. An analysis of the Burnett equations based on the second law of thermodynamics. (AIAA 95-0415), 1995.

[10] James B. Starr. Squeeze-film damping in solid-state accelecrometers. In *1990 Solid-State Sensor and Actuator Workshop*, pages 44–47, Hilton Head, June 1990.

[11] S.B. Choi, R.F. Barron, and Warrington R.O. Fluid flow and heat transfer in microtubes. In *Micromechanical Sensors, Actuators, and Systems, ASME Winter Annual meeting*, pages 123–133, Atlanta, GA, December 1991.

[12] A. Padmanabhan, H.D. Goldberg, K.S. Breuer, and M.A. Schmidt. A silicon micromachined floating-element shear-stress sensor with optical position sensing by photodiodes. In *The 8th international conference on solid-state sensors and actuators Eurosensors (IX)*, pages 436–439, Stockholm, Sweeden, June 25-29 1995.

[13] M. Andrews and I. Harris. Damping and gas viscosity measurements using a microstructure. *Sensors and Actuators*, (49):103–108, 1995.

[14] D. Pan, T. Hyman, M. Mehregany, E. Reshotko, and Willis B. Calibration of microfabricated shear stress sensors. In *The 8th international conference on solid-state sensors and actuators Eurosensors (IX)*, pages 443–446, Stockholm, Sweeden, June 25-29 1995.

[15] J.J. Yao and M.F. Chang. A surfaced micromachined miniature switch for telecommunications applications with signal frequencies from dc to 4 ghz. In *Transducers '95*, pages 384–387, Stockholm, Sweden, June 1995.

[16] J.C. Harley, Y. Huang, H.H. Bau, and Zemel J.N. Gas flow in micro-channels. *Journal of Fluid Mechanics*, 284:257–274, 1995.

[17] E.B. Arkilic, M.A. Schmidt, and K.S. Breuer. Slip flow in mircochannels. In J Harvey and G Lord, editors, *Rarefied Gas Dynamics*. Oxford University Press, Oxford, England, 1995.

[18] F.O. Goodman and H.Y. Wachman. *Dynamics of Gas-Surface Scattering*. Academic Press, New York, 1976.

[19] J.C. Maxwell. *The Scientific Papers of James Clerk Maxwell*. Dover Pulications, Inc., New York, New York, 1965.

[20] A. Beskok and G.E. Karniadakis. Simulation of heat and momentum transfer in micro-geometries. (AIAA 93-3269), 1993.

[21] Errol Arkilic. Gaseous flow in micron-sized channels. Master's thesis, Massachusetts Institute of Technology, Cambridge, MA, January 1994.

[22] E. Steinheil, M. Scherber, and M. Seidl. Investigations on the interaction of gases and well-defined solid surfaces with respect to possibilities for reduction of aerodynamic friction and aerothermal heating. In J. Potter, editor, *Rarefied Gas Dynamics*. American Institute of Aeronautics and Astronautics, 1977.

[23] L.B. Thomas and R.G. Lord. Comparative measurements of tangential momentum and thermal accommodations on polished and on roughened steel spheres. In K. Karamcheti, editor, *Rarefied Gas Dynamics*. Academic Press, New York, New York, 1974.

[24] M. Seidl and E. Steinheil. Measurement of momentum accommodation coefficients on surfaces characterized by Auger spectroscopy, Sims and LEED. In M. Becker and M Fieberg, editors, *Rarefied Gas Dynamics*. DFVLR Press, 1974.

[25] B.T. Porodnov, P.E. Suetin, S.F. Borisov, and V.D. Akinshin. Experimental investigation of rarefied gas flow in different channels. *Journal of Fluid Mechanics*, 64:417–437, 1974.

[26] A.V. Nakarjakov, S.F. Borisov, F.M. Sharipov, and P.E. Suetin. The effect of the surface chemical composition on a free molecular gas flow in a cylindrical channel. In J. Harvey and G. Lord, editors, *Rarefied Gas Dynamics*. Oxford University Press, Oxford, 1995.

[27] R.H. Edwards. Low density flows through tubes and nozzles. In J. Potter, editor, *Rarefied Gas Dynamics*. American Institute of Aeronautics and Astronautics, New York, New York, 1977.

[28] G. Pham-Van-Diep, P. Keely, E.P Muntz, and D.P Weaver. A micromechanical Knudsen compressor. In J Harvey and G Lord, editors, *Rarefied Gas Dynamics*. Oxford University Press, Oxford, England, 1995.

[29] E.B. Arkilic, M.A. Schmidt, and K.S. Breuer. Gaseous flow in microchannels. In *Application of Microfabrication to Fluid Mechanics, ASME Winter Annual meeting*, pages 57–65, Chicago, Ill., Nov 1994.

[30] K.C. Pong, C.M. Ho, Liu J., and Y.C. Tai. Non-linear pressure distribution in uniform microchannels. In *Application of Microfabrication to Fluid Mechanics, ASME Winter Annual meeting*, pages 51–56, Chicago, Ill., Nov 1994.

[31] E.S. Piekos and K.S. Breuer. DSMC modeling of micromechanical devices. (AIAA 95-2089), 1995.

[32] R. Prud'homme, T. Chapman, and J. Bowen. Laminar compressible flow in a tube. *Applied Scientific Research*, (43:67-74), 1986.

[33] H.R. van den Berg, C.A. Seldam, and P.S. Gulik. Compressible laminar flow in a capillary. *Journal of Fluid Mechanics*, (246:1-20), 1993.

[34] J.C. Shih, C. Ho, J. Liu, and Y. Tai. Monatomic and polyatomic gas flow through uniform microchannels. In *Application of Microfabrication to Fluid Mechanics, ASME Winter Annual meeting*, pages 197–203, Atlanta, Ga., Nov 1996.

[35] F. M. White. *Viscous Fluid Flow.* McGraw-Hill, Inc, New York, New York, 1991.

[36] J. Pfahler, J. Harley, H. Bau, and J. Zemel. Gas and liquid flow in small channels. In *Micromechanical Sensors, Actuators, and Systems, ASME Winter Annual meeting*, pages 49–59, Atlanta, GA, December 1991.

[37] M.A. Schmidt. Silicon wafer bonding for micromechanical devices. In *Solid State Sensor and Actuator Workshop*, pages 127–131, Hilton Head, June 1994.

[38] D.K. Cohen and R. Nieman. Non-contact measurement of polished silicon wafer microroughness. Technical Report 91-011, Wyko Corporation, December 1991.

[39] S.A. Tison. Low-flow calibration system. In *Proceedings of the 40th International Instrumentation Symposium*, pages 571–578, Blatimore, MD, 1994.

[40] Stuart Tison. Personal communication.

[41] K. McCulloh, C. Tilford, and F. Long. Low-range flow meters for use with vacuum and leak standards. *Journal of Vacuum Sciences and Technology A*, (5.3), 1987.

[42] M Bergoglio, A. Calcatelli, and G. Rumiano. Gas flowrate measurements for leak calibration. *Vaccum*, 46(8-10):763–765, 1995.

[43] T. Gabrielson. Mechanical-thermal noise in micromachined acoustics and vibration sensors. *IEEE Transactions on Electron Devices*, 40(5):903–909, 1993.

[44] MKS Techical Support. Andover Massachusetts. Personal communication.

[45] H.W. Coleman and W.G. Steele. *Experimentation and Uncertainty Analysis for Engineers.* John Wiley and Sons, New York, New York, 1989.

[46] Chi-Ming Ho. Personal communication.

[47] John Harley. Personal communication.

[48] James E John. *Gas Dynamics.* Allyn and Bacon, Boston, MA, 1984.

[49] D McQuarrie and P Rock. *General Chemistry.* W.H. Freeman and Company, New York, New York, 1984.

[50] J. Hilsenrath and *et al.* Tables of thermodynamic and transport properties,. *Nat. Bur. Std. Circular 564*, 1955.

[51] S. Timoshenko and S. Woinowsky-Krieger. *Theory of Plates and Shells, second edition.* McGraw-Hill, New York, New York, 1959.